Four Measures of the Intracluster Medium Temperature and their Relation to a Cluster's Dynamical State

B. F. Mathiesen
Dept. of Physics, Stanford University, Stanford, CA 94305 USA

A. E. Evrard
Dept. of Physics, University of Michigan, Ann Arbor, MI 48109-1120 USA

ABSTRACT

We employ an ensemble of 24 hydrodynamic cluster simulations to create spatially and spectrally resolved images of quality comparable to *Chandra*'s expected performance. Emission from simulation mass elements is represented using the XSPEC `mekal` program assuming 0.3 solar metallicity and the resulting spectra are fit with a single-temperature model. Despite significant departures from isothermality in the cluster gas, single-temperature models produce acceptable fits to 20,000 source photon spectra. The spectral fit temperature T_s is generally lower than the mass weighted average temperature T_m due to the influence of soft line emission from cooler gas being accreted as part of the hierarchical clustering process.

The nature of this deviation depends on the bandpass used for spectral fitting. In a *Chandra*-like bandpass of 0.5 to 9.5 keV we find a nearly uniform fractional bias of $(T_m - T_s)/T_s \simeq 20\%$, although smaller clusters sometimes demonstrate much greater deviations. If the minimum energy threshold is raised to 2 keV, however, the effect of line emission on the spectrum is greatly decreased and T_s becomes a nearly unbiased estimator of T_m for smaller clusters. The fractional deviation in T_s relative to T_m is scale-dependent in this bandpass and follows the approximate relation $(T_m - T_s)/T_s = 0.2 \log_{10} T_m$. This results in an observed M_{ICM}–T_s relationship for the simulations with slope of about 1.6, intermediate between the virial relation $M \propto T_m^{3/2}$ and the observed relation $M_{\rm ICM} \propto T^2$.

Tracking each cluster in the ensemble at 16 epochs in its evolutionary history, we catalogue merger events with mass ratios exceeding 10% in order to investigate the relationship between spectral temperature and proximity to a major merger event. Clusters that are very cool relative to the mean mass-temperature relationship lie preferentially close to a major merger, suggesting a viable observational method to cull a subset of dynamically young clusters from the general population.

Subject headings: cosmology: observations — galaxies: clusters: general — intergalactic medium — X–Rays: general

1. Introduction

Galaxy clusters are the youngest and largest organized structures in the universe, and as such provide us with a wealth of cosmological information. The most massive clusters draw their substance from cosmologically significant volumes of linear scale $\gtrsim 10h^{-1}$ Mpc. These scales are large enough that no known coherent process competes against gravity, so rich cluster contents are thought to comprise a fair sample of the universe's ingredients (White *et al.* 1993). Because clusters are rare nonlinear excursions of

the cosmic density field, the statistical properties of their population are quite sensitive to both cosmological model and slope of the primordial fluctuation spectrum. Unfortunately, their relative youth can also make interesting physical properties difficult to measure: about 50% of the local population bears evidence of ongoing mergers, and the canonical "relaxed" cluster is a relatively rare beast.

Nearly all interesting cosmological tests depend on accurate measurement of cluster virial masses. Observations of the intracluster medium (ICM) have shown promise in this regard: the ICM's high X-ray luminosity and large spatial extent make it possible to probe the content and structure of clusters in great detail. Bulk properties of the ICM such as luminosity, temperature, mass, and gas density profile shape have been found to display highly significant correlations with each other (Edge & Stewart 1991; David *et al.* 1993; Mohr & Evrard 1997; Mushotzky & Scharf 1997; Markevitch 1998; Allen & Fabian 1998; Mohr, Mathiesen & Evrard 1999; Arnaud & Evrard 1999). In contrast to the noisy correlations of early X-ray data (Sarazin 1986 and references therein), many correlations now display scatter at the $10-20\%$ level, indicating that a high degree of physical uniformity exists even in this structurally diverse population. Hydrodynamic simulations of cluster evolution predict tight relationships between observable quantities and between those quantities and the cluster binding mass (Evrard 1990; Kang *et al.* 1994; Navarro, Frenk & White 1995; Evrard *et al.* 1996; Bryan & Norman 1998), even when some members of the sample are far from dynamical equilibrium. The existence of both observed and theoretical correlations implies that the prevalence of cluster substructure is not a fundamental barrier to interpreting the properties of the population.

However, moderate biases caused by the presence of substructure are likely to be present, and we explore the role of substructure in temperature measurements of the ICM in this paper. A previous paper (Mathiesen, Evrard & Mohr 1999) demonstrated that a ICM clumping leads to a modest ($\sim 15\%$) overestimate of ICM masses derived under the typical assumptions of spherical symmetry and isothermality. As the X–ray data improve, the limits of simplifying assumptions such as these become clearer. High-resolution X–ray images reveal secondary peaks and strong asphericities in many clusters and X–ray spectra indicate the presence of multiple temperature components within the cores of many clusters (Fabian *et al.* 1994, Holzapfel *et al.* 1997, Allen *et al.* 2000). The *Chandra* and *XMM* satellite missions will provide the most detailed maps of the ICM emission and temperature structure yet obtained and will allow more precise definition of the limitations of the current models.

Three-dimensional hydrodynamical simulations of cluster formation can help bridge the gap between the new generation of data and traditional methods and results. While simulated clusters often do not include many processes thought to be important to ICM evolution (e.g. radiative cooling and galactic winds), they excel at the creation of populations with realistic merger histories (Mohr *et al.* 1995; Tsai & Buote 1996). Ensembles of simulated clusters can therefore be used to investigate the effects of accretion events, major mergers, clumping, and substructure on measurements of the ICM. In this paper, we analyze the spectral properties of an ensemble of 24 simulated clusters using a realistic plasma emission model and assuming a uniform metallicity 0.3 times the solar abundance. We find that even minor accretion events can significantly bias our measurements of the mean, mass-weighted cluster temperature, and that clusters undergoing a major merger can sometimes be identified as extreme examples of this bias.

Section 2 of this paper describes the simulations, the cluster ensemble, and the process of creating our spectral images. Section 3 discusses the various measures of cluster temperature which have seen frequent use and explores the relationships between them. In particular we explore the relationship between spectrally determined temperatures and the mass-weighted mean temperature. The latter is found in simulations to follow most closely the virial relationship. Section 4 then delves into cluster dynamics,

investigating the effects of a major merger on the ICM and looking for observable signatures of the merging process. Finally, section 5 summarizes our conclusions.

2. Simulations

We use an ensemble of 24 hydrodynamical cluster simulations, divided evenly between two reasonable cold dark matter (CDM) cosmological models. These models are (i) OCDM ($\Omega_0 = 0.3$, $\sigma_8 = 1.0$, $h = 0.8$, $\Gamma = 0.24$); and (ii) ΛCDM ($\Omega_0 = 0.3$, $\lambda_0 = 0.7$, $\sigma_8 = 1.0$, $h = 0.8$, $\Gamma = 0.24$). Here the Hubble constant is $100h$ km s^{-1} Mpc^{-1}, and σ_8 is the linearly evolved, present power spectrum normalization on $8h^{-1}$ Mpc scales. The initial conditions are Gaussian random fields consistent with a CDM transfer function with the specified Γ (e.g. Bond & Efstathiou 1984). The baryon density is set in each case to 20% of the total mass density ($\Omega_b = 0.2\Omega_0$). The simulation scheme is P3MSPH; first a P^{3}M (DM only) simulation is used to find cluster formation sites in a large volume, then a hydrodynamic simulation is performed on individual clusters to resolve their DM halo and ICM structure in detail. The baryonic component is modeled with 32^3 particles, providing a typical mass resolution of 0.01% within the virial radius. The resulting cluster sample covers a little more than a decade in total mass, ranging from about 10^{14} to $3 \times 10^{15} M_\odot$. Further details on these simulations can be found in Mohr & Evrard (1997).

The simulations model the dynamical and thermodynamical effects of gravitation, shock heating and adiabatic work on the ICM. Several potentially important pieces of physics are neglected. Radiative cooling is one; our clusters cannot produce cooling flows in their cores. These are inferred to be quite common in the population (Edge & Stewart 1991, White *et al.* 1997), and many methods have been presented in the literature for removing the effects of cooling flows from measurements of bulk ICM properties. We expect that the new satellites *Chandra* and *XMM* will be able to directly observe the spatial extent of cooling flows and simply remove those pixels if desired. We thus analyze our simulations under the assumption that they are comparable to real ICM observations correct for the presence of cooling flows through excision (e.g. Markevitch *et al.* 1998) or explicit modeling (e.g. Allen *et al.* 2000) of the extra emission component. We also lack any treatment of ICM evolution through galaxy interactions such as supernova enrichment. Instead, we assume that the abundance of heavy elements is constant throughout a cluster's history. The heating effects of galactic winds are difficult to parameterize accurately, and we postpone this investigation to a future set of numerical experiments including an approximate version of galactic feedback.

It also has been proposed that the ICM electron temperature lags behind the ion temperature to a significant degree, an effect which occurs due to the long equipartition timescale for plasmas with typical ICM densities and temperatures. This view has been supported by observation of ASCA temperature profiles (Markevitch *et al.* 1996), analytical modeling of accretion shocks (Fox & Loeb 1997), and hydrodynamical simulation of the formation of a rich cluster (Chièze, Alimi & Teyssier 1998; Takizawa 1999). The latter show that the effect is small ($\lesssim 10\%$) except in the outer regions of the most massive clusters. Our simulations, which treat the ICM as a single thermodynamic fluid, do not take into account this effect. Allowing cooler electron temperatures in the outskirts of clusters would increase the magnitude of the spectral effects calibrated below.

2.1. Spectral image generation

From the simulation output, observables such as X–ray spectra and surface brightness maps are obtained as follows. Each simulation particle is given a model for its X–ray emission based on its local ion density n_i and thermodynamic temperature T_i. Previous works have traditionally used a simple Bremsstrahlung-based model such as $\epsilon_i \propto n_i^2 T_i^{1/2}$, but we employ the more sophisticated `mekal` model from the XSPEC utility (Mewe *et al.* 1986; a URL for the XSPEC user's manual is also in the bibliography). The `mekal` spectra are created using 0.3 solar abundance for elements heavier than hydrogen. Each cluster is "viewed" along a single axis, and a subvolume of the simulation containing the cluster is divided into image pixels. Each particle's emission is collected into the image and smoothed over neighboring pixels with a Gaussian function of the same width as that particle's SPH smoothing kernel. The resultant "data cube" contains a spectrum at each "sky" position. To our knowledge, this is the first such spectral visualization of a simulated intracluster medium.

The particle data are output at twenty time intervals over the entire simulation, equally spaced in cosmic time. Groups are identified at each epoch using a friends-of-friends algorithm with linking parameter 0.15 the mean interparticle separation. This procedure connects particles having separations corresponding to roughly $\gtrsim 400$ times the background density (Lacey & Cole 1994). The position of each group is taken to be that of the dark matter particle with the minimum gravitational potential; this point is always used as the image center. We have created a catalogue of "major merger" events for each cluster by identifying all instances of groups with two or more progenitors having a mass ratio $\geq 10\%$. The entire sample contains 75 such events. Images are created for the last 16 outputs along a single viewing direction, resulting in a total of $16 \times 24 = 384$ observable physical states. In certain specified situations we use a subset of these outputs, focusing on the images corresponding to redshifts about equal to 0, 0.5, and 1 for each cluster. The full evolutionary histories of the clusters are used to enhance the variation of substructure in our sample and provide insight into the effects of mergers on the ICM's observable characteristics.

Our primary database consists of two spectral cubes for each output differing only in radial scale. We choose half-widths of r_{500} and r_{200} in the plane of the sky, and line-of-sight depth of $2r_{200}$. The scale r_Δ is the radius at which the mean interior density contrast falls to Δ times the critical density $\rho_c \equiv 3\mathrm{H_o}^2/8\pi\mathrm{G}$ at the viewing epoch. The smaller radius r_{500} corresponds roughly to the readily visible portion of current observations, while r_{200} is the theoretical preference for the virial radius of clusters in an $\Omega = 1$ cosmology. We used scaled radii rather than a fixed metric radius in order to probe regions with similar dynamical character. Each image uses the `mekal` spectral model for the ICM X–ray emission, and contains a 256-pixel spatial image of the cluster for each energy bin. The model spectra have a bin size of 100 eV and bandpass of [0.1,20] keV, allowing a great deal of flexibility in producing spectra comparable to observations. The spectral cubes created for this work have a bin size of 150 eV and a bandpass of [0.5,9.5] keV in order to simulate the quality of data expected from *Chandra's* Advanced CCD Imaging Spectrometer (ACIS). A color figure (Table 2) displaying X-ray surface brightness and spectral temperature images in two different bandpasses is presented and discussed in section 4.1, but the reader may wish to glance at it now to get a visual impression of the data used in this paper.

As we will see, our use of a spectral model for ICM emission has important consequences. Previous X–ray images derived from simulations use a simple Bremsstrahlung model, but line emission can make up as much as 20% of the cluster luminosity for gas at relatively low ($\lesssim 2.0$ keV) temperatures. While continuum emission in the low energy ROSAT passband is a weak function of temperature above this threshold (Mohr *et al.* 1999), the introduction of line emission into the model brings a strong temperature

dependence back into the soft X–rays. This effect can be seen in Figure 1, which plots isothermal mekal spectra with 0.3 solar abundance at temperatures typical of the ICM. Since soft ($E < 2$ keV) line emission is progressively more pronounced at cooler temperatures, even a small amount of cold gas in the observation window can make a spectrum appear significantly cooler. This effect is central to the results presented in this paper.

3. Temperatures

Cluster atmospheres are only approximately, never identically, isothermal. Description of the ICM by a single temperature T is not only incomplete but also dependent on the measure employed to derive the value of T. Common definitions employed in the literature use the mass-weighting and an approximate emission-weighting methods described below.

With Lagrangian simulations, volume integrals tranform to sums over particles within the volume

$$\int dV\, \rho^n\, T \;\longrightarrow\; \sum_i m_i\, \rho_i^{n-1}\, T_i \tag{1}$$

where m_i is the mass and ρ_i and T_i the density and temperature of the $i^{\rm th}$ particle. Our simulations employ equal mass gas particles, so the mass-weighted temperature within r_Δ is a simple average over N SPH particles

$$T_m \;=\; \frac{1}{N}\sum_i^N T_i, \tag{2}$$

while the approximate emission-weighted temperature employs a ρ^2 volume weighting that transforms to

$$T_e \;=\; \sum_i^N \rho_i T_i \,/\, \sum_i^N \rho_i \tag{3}$$

in a Lagrangian implementation. Somewhat more sophisticated implementations of emission-weighting have been employed; for example, Evrard, Metzler & Navarro (1996) use a ROSAT emission weighting measure that incorporates the temperature dependence of bremsstrahlung emission within an $0.1 - 2.4$ keV energy passband. Within the simulations, we determine both T_m and T_e within spherical boundaries of radii r_{500} and r_{200}.

If cluster atmospheres within r_Δ are hydrostatic and in virial equilibrium, then the thermal energy of the ICM will reflect the net gravitational potential energy of the cluster. This leads to the oft-cited virial relation between mass-weighted temperature and binding mass

$$kT_m \;=\; \alpha G M_\Delta / r_\Delta \tag{4}$$

where M_Δ is the total mass within a sphere of radius r_Δ and α is a dimensionless form factor. Assuming that α is a constant independent of mass and redshift (strict self–similarity) and recalling that $M_\Delta(z) \propto \Delta\rho_c(z) r_\Delta^3$ with $\rho_c(z) \propto H^2(z)$, we arrive at a compact form for the virial mass-temperature relation

$$h(z) M_\Delta \;\propto\; T_m^{3/2} \tag{5}$$

with $h(z) = H(z)/100$ km s^{-1} Mpc^{-1}. The factor $H(z)$ takes into account the cosmological scaling of this relationship, and can be derived from the Friedmann equation. For the flat universe modeled in

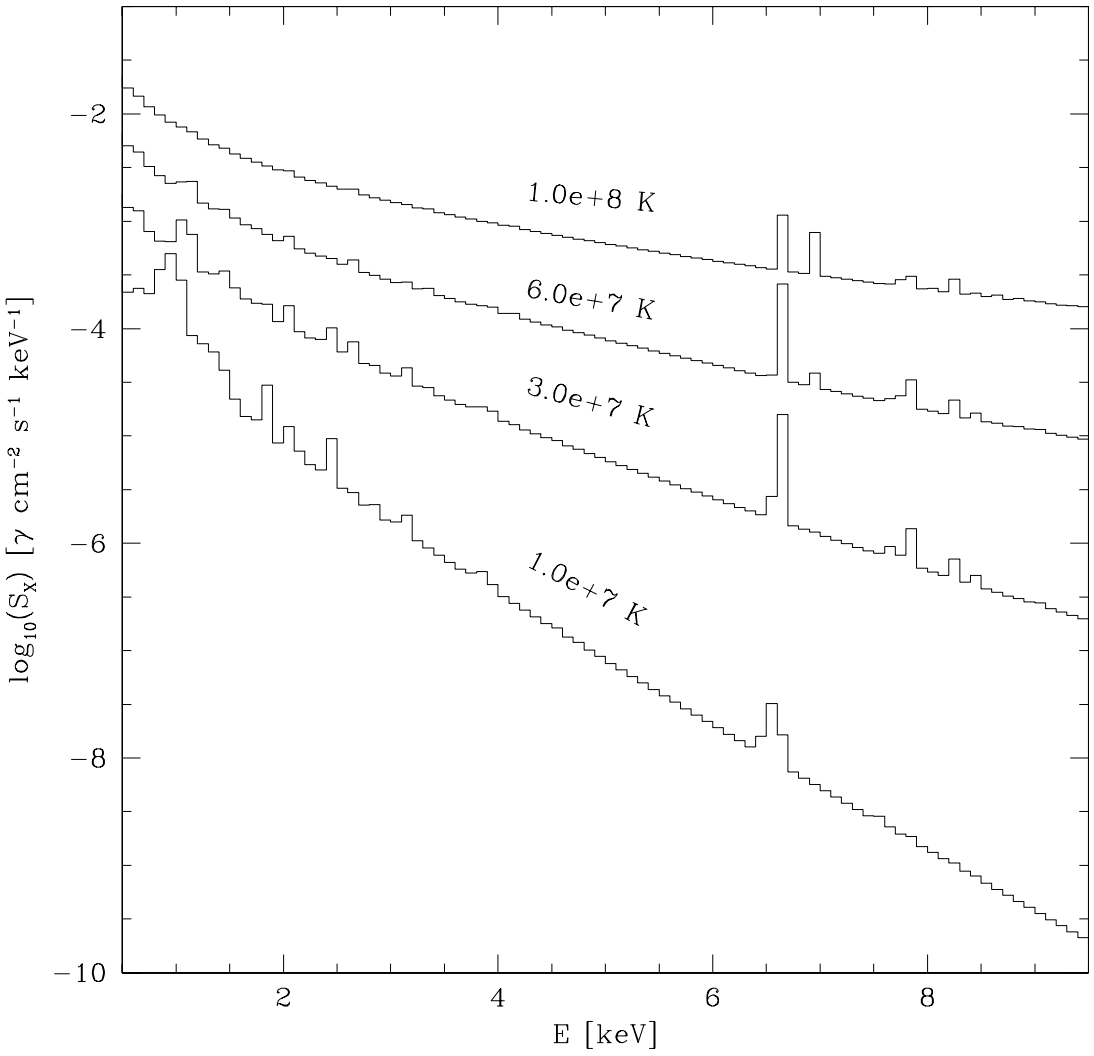

Fig. 1.— Sample mekal spectra at 0.3 solar abundance. The 1.0×10^8 K (8.6 keV) spectrum is plotted in its true units on the y-axis, while the cooler spectra are scaled downward by factors of 4 (6.0×10^7 K), 16 (2.0×10^7 K), and 100 (1.0×10^7 K). These temperatures correspond to kT = 8.6, 5.2, 1.7, and 0.86 keV. The flux was calculated assuming a 1 Mpc^3 volume of gas with hydrogen density 10^{-3} cm^{-3} at a distance of 225 Mpc.

our simulations, $(H(z)/H_0)^2 = [\Omega_{\rm m}(1+z)^3 + \Omega_\Lambda]$, where $\Omega_\Lambda = \Lambda/3H_0^2$. This factor is equivalent to the evolution factor $E(z)$ used by Bryan & Norman (1998).

This relationship determined at $\Delta = 500$ is presented in Figure 2 using three simulation outputs for each cluster at the redshifts $z = 1$, 0.5 and 0. The data agree well with the virial expection; the best-fit power law

$$h(z)M_{500} = (1.2 \pm 0.1) \times 10^{15} (T_m/10 \text{ keV})^{1.52\pm0.03} [\mathrm{M}_\odot] \quad (6)$$

exhibits only 14% scatter in mass at fixed T_m. The data within $\Delta = 200$ have a similar slope and slightly larger scatter.

Results such as these have led many cosmologists to use the virial relation, calibrated by simulations or a well-studied nearby cluster, to estimate binding masses from cluster temperatures. Even if current simulations are complete and exact in their physical description of the ICM, this procedure need not be correct, since the mass-weighted temperature is not a directly obervable quantity. Computational cosmologists have often employed the simplified emission-weighted temperature T_e in an effort to move closer to observations. What is actually measured, however, is a spectral temperature derived from fitting a single Raymond-Smith or `mekal` model to the spectral data of a cluster. Papers analyzing a single cluster or a small sample sometimes employ two temperature components and/or a model cooling flow spectrum in order to improve the fit. These variations are physically well-motivated but often unnecessary in the sense that a single temperature component usually provides an acceptable fit to even high quality spectral data (Holzapfel *et al.* 1997).

3.1. Spectral Temperatures

From the simulations, we produce spectral temperatures by fitting isothermal models to sample photon spectra. The latter are produced by summing emission from gas within a cylinder of appropriate radius and depth $2r_{200}$ centered on the cluster. This collection volume includes most of the line-of-sight gas in the simulation, but projection effects from large-scale structure (represented in the high-resolution simulation by massive dark matter particles with no associated baryons) are not taken into account. The combined spectrum is rebinned into channels of width 150 eV (comparable to the *Chandra* ACIS energy resolution), convolved with the *Chandra* effective area function, and assigned Poisson error bars appropriate to the number of photons in each bin, assuming a total photon count of 20,000. Bins with a low count rate are grouped together until they contain at least twenty photons. The result is then fit to a single-temperature `mekal` spectrum with 0.3 solar metallicity. No Poisson *noise* is added to the photon counts, as we are trying to isolate the systematic effects of substructure, but the error bars are used in fitting to assign appropriate relative weights to the data. The resulting spectral temperature T_s which minimizes the chi-squared (the normalization of the spectrum is also a free parameter, of course) is a direct analog of observed temperatures obtained by the *Chandra* observatory. Other satellites can readily be simulated by changing the bin width, bandpass, and effective area function.

A sample of this process is shown in Figure 3, which displays the combined spectrum, best-fit spectrum, and residuals for a typical cluster of the ensemble. Although this spectrum is formally well fit by a single-temperature model, there are clear trends in the residuals: the strength of the iron line is somewhat too low for a continuum with this slope, the width of the iron line is increased somewhat from the lower-energy transitions in this complex, the 1.0 keV bin is much too high, and the overall shape of the spectrum is slightly different. With the exception of the iron line and the 1.0 keV bin these excursions

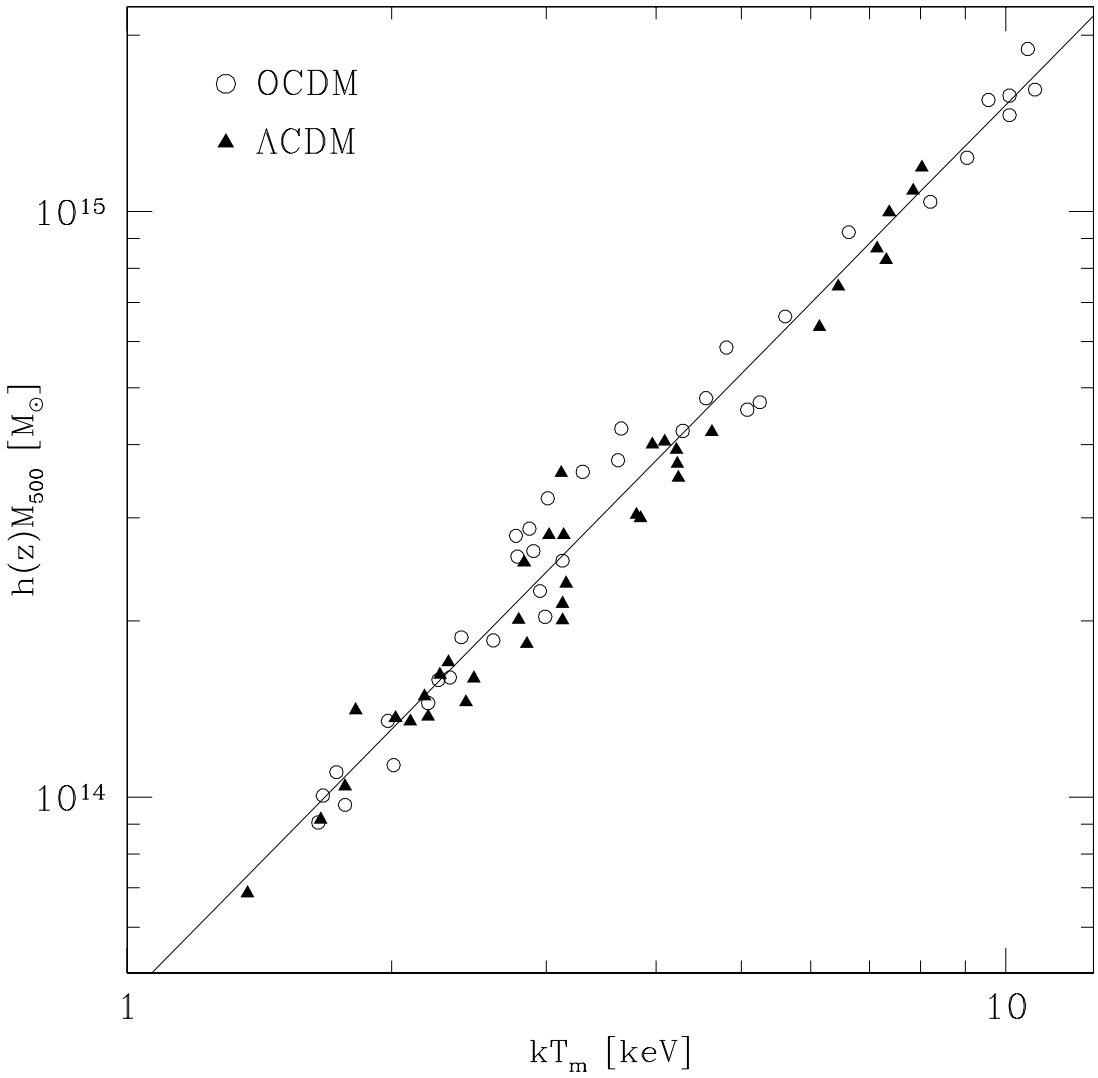

Fig. 2.— The virial mass-temperature relationship within r_{500} for simulated clusters. The solid line represents the least-squares fit to the data given in equation 6. Three output frames per simulation are included in the plot, corresponding to the redshifts of 0, 0.5, and 1.0.

are very small, and we would not expect them to be visible in a real spectrum with this photon count and typical noise levels. Deep exposures from *Chandra* might be able to pick them out, however. Increasing the photon count to 100,000 for this cluster brings the reduced chi-squared up to 1.64 for 54 degrees of freedom, enough to detect the difference in spectral shape even with typical levels of random error. The unusual coincidence that a realistic combined spectrum has nearly the same shape as an isothermal spectrum may be explained by our mediocre energy resolution, which keeps us from constraining the structure of the emission lines to a useful degree.

We have cut off the spectrum at 9.5 keV due to a lack of photons above this range. The spectral temperatures are significantly lower than both the emission- and mass-weighted temperatures for this cluster. The reasons for these differences are related to this particular cluster's dynamical state. In Figure 4, we show a phase diagram of the ICM gas within r_{200} the cluster center. The tongue of low temperature material is a small merging subclump that is barely visible in the X–ray surface brightness. We have drawn a horizontal line at 2.2 keV ($\log T$ [K] = 7.4) to visually separate the core of this subclump. Particles below this threshold (and especially those in the clump, which is nearly as dense as the cluster core) produce significant line emission in the [0.5,2.0] keV band and enhance the spectrum in this region. Only 4% of the particles in the cluster lie below this line, but it turns out that this is more than enough to significantly alter the shape of the spectrum. The dashed lines in Figure 4 represent the minimum entropy thresholds inferred by Lloyd-Davies, Ponman, & Cannon (2000) from X–ray observations of galaxy groups, and will be discussed further at the end of section 3.2.

This is an important point: minor mergers such as this are just as likely as major events to cause deviations between the spectral and mass-weighted temperatures. Not only are they much more common, their gas is colder—and therefore more luminous in the soft X–ray band.

We find that this bias is nearly universal in our sample, and are motivated to construct the mutual correlations of the three temperatures. These relationships are displayed in Figure 5. The spectral temperatures occur at discrete intervals because we tabulated `mekal` outputs at temperatures with spacing $\Delta \log T = 0.02$ in all our analysis (at considerable savings in CPU time). This interval is much smaller than the uncertainties associated with our spectral temperatures. The constants a and b displayed in the plots result from fits $T_y = bT_x^a$ obtained by least-squares linear regression using logarithmic variables.

We can see from these plots that the mass- or emission-weighted temperatures are almost universally higher than the spectral temperatures. Why is this the case? The mass-weighted temperatures, as we have seen, follow the virial expectation quite closely and can be used as a benchmark for the cluster's evolution. The emission-weighted temperatures strongly favor the core region, so also tend to mark the potential well depth rather well. The spectral temperature, on the other hand, is weighted by the fitting process towards whichever regions emit the most photons. This favors both high-density regions and cool regions, and the cores of accreting subclumps satisfy both criteria. Accreting clumps of cool gas can therefore create an excess of soft photons for some time during and after a merger event. This process will be discussed in more detail in section 4, but for now it suffices to realize that accretion and substructure can have a rather large effect on spectral temperatures. T_s doesn't change a great deal when we go from r_{200} to r_{500}, but the mass-weighted temperature increases; this is why we see a larger bias within r_{500} despite the fact that the former window includes a larger volume of cool gas.

Is there evidence of this phenomenon in the literature? Accurate temperature determinations for clusters are available from the satellites *Einstein*, *EXOSAT*, *Ginga*, and *ASCA*, each of which uses a different bandpass in fitting their X–ray spectra. We can test for the presence of the effect described here

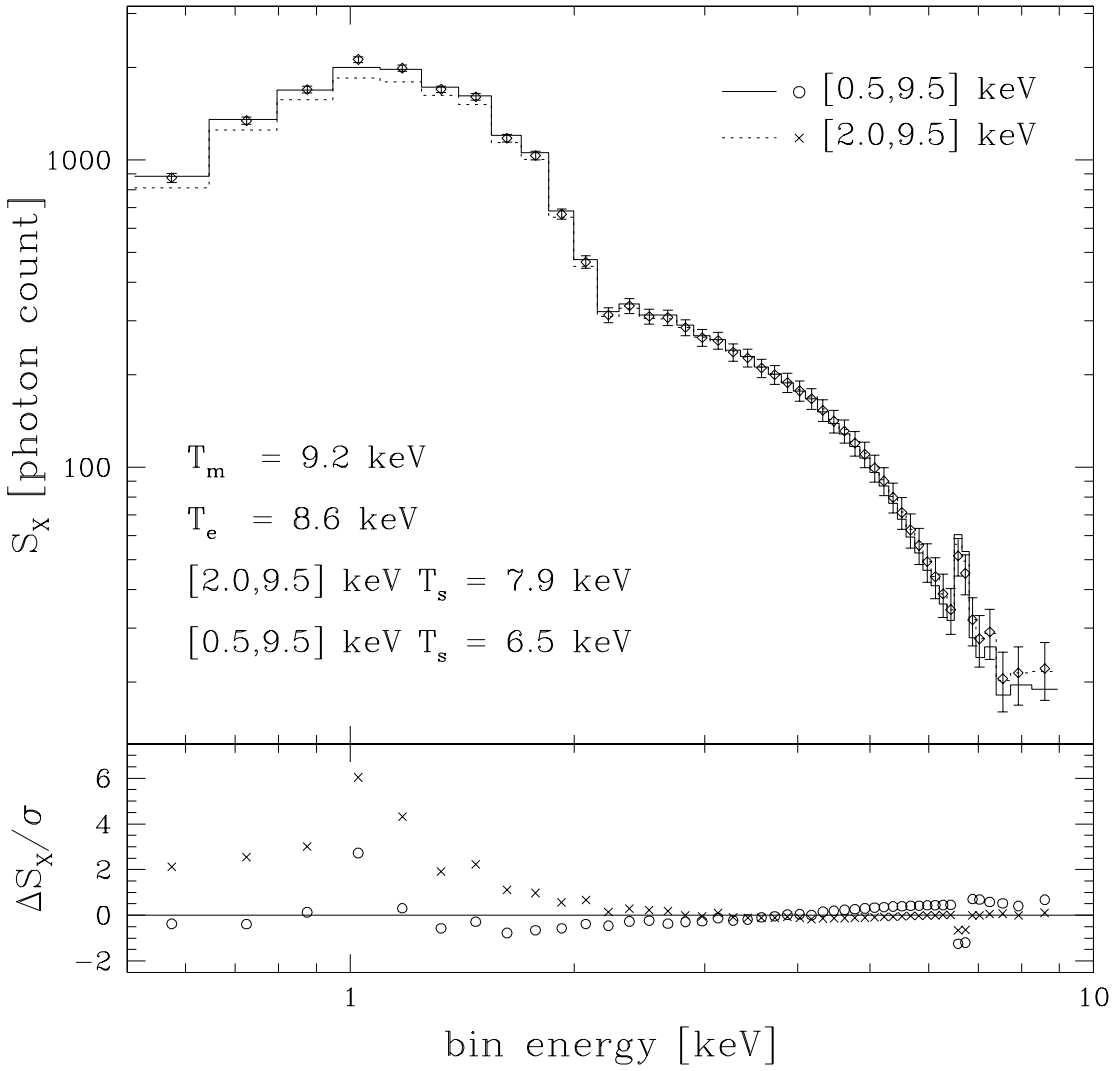

Fig. 3.— Simulated *Chandra* spectrum for a rich cluster at redshift of 0.042. The photons are collected within a cylinder of diameter and depth r_{200} centered on the minimum potential of the simulation. The exposure time is scaled so that the spectrum contains approximately 20,000 photons, but the best-fit temperatures obtained are insensitive to the total photon count. Two isothermal mekal spectra are displayed: the solid line is the best fit for all the bins, and the dotted line is the best fit that results for bins over 2 keV. The reduced chi-squared parameters for the two models are $\chi^2/46 = 0.38$ for the full spectrum and $\chi^2/36 = 0.05$ for the fit to bins above 2 keV.

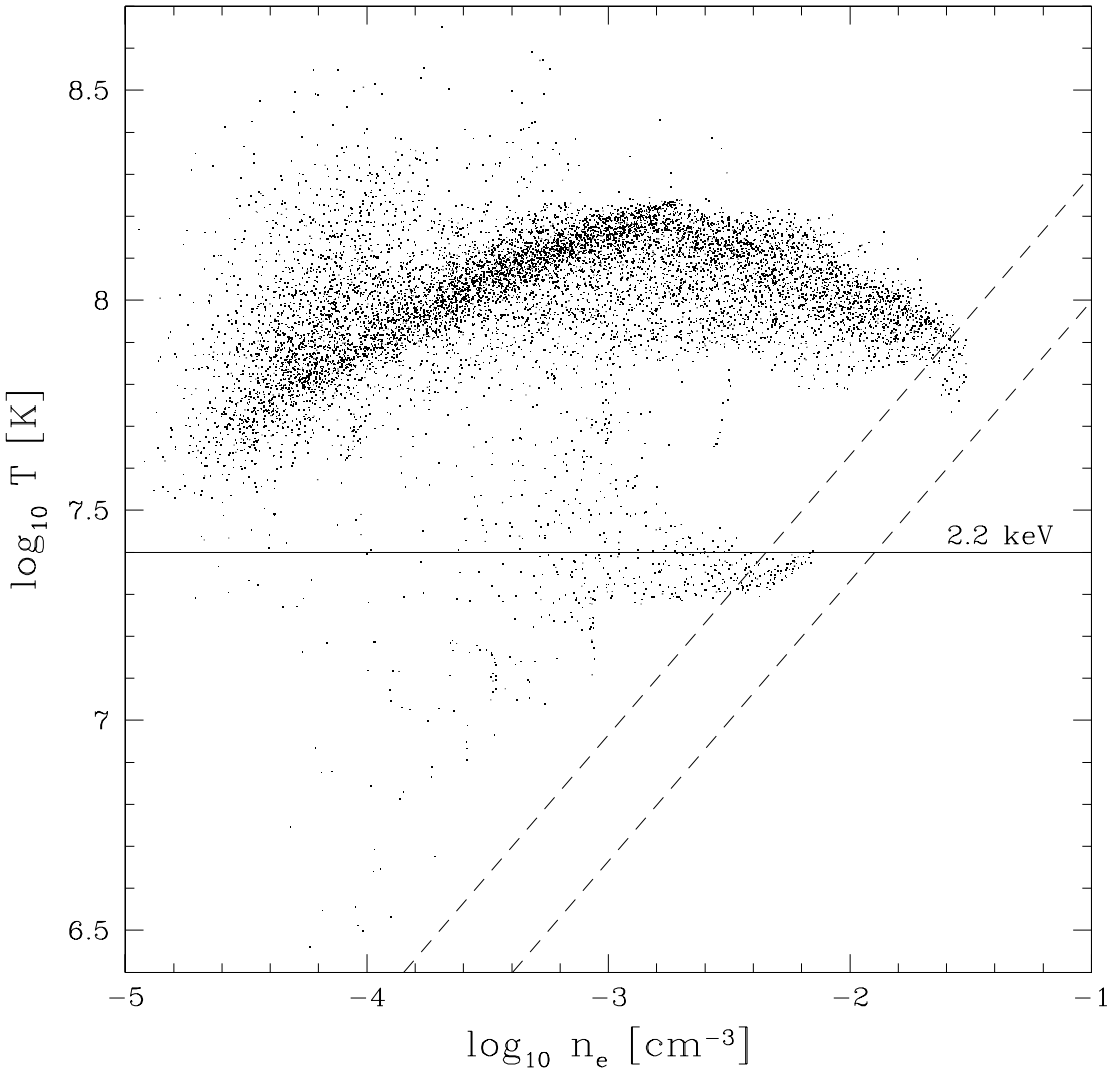

Fig. 4.— Phase-space diagram showing the local temperature and number density of particles lying within r_{200} of the cluster whose spectrum is displayed in Figure 3. The horizontal line is drawn to separate out the merging subclump and indicate an approximate threshold for significant line emission in the [0.5,2.0] keV band. Particles below this line make up only 4% of the total mass, but cause a 30% shift in the spectral temperature. The dashed lines represent minimum entropy thresholds of 40 and 80 keV cm^2 (Lloyd-Davies *et al.* 2000); if the ICM were preheated prior to cluster formation infalling subclumps would be tend to be more diffuse.

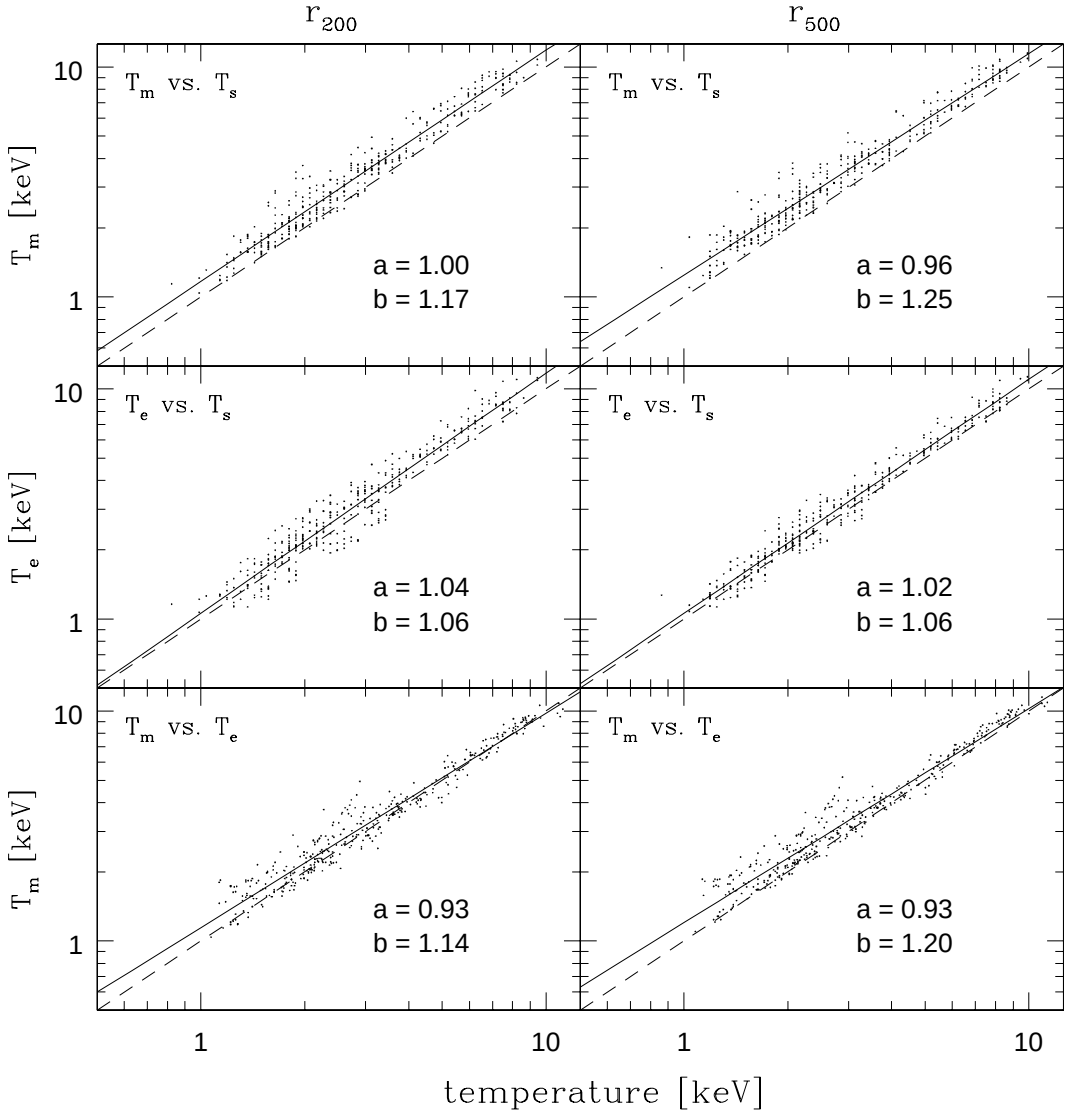

Fig. 5.— Correlations between spectral, mass-weighted, and emission-weighted temperatures for 384 simulation outputs (24 different clusters). Spectral temperatures have been fit in the 0.5-9.5 keV band. The left column shows measurements within the virial radius r_{200} while the right column uses measurements within r_{500}. The coefficients a and b relate the x and y coordinates as $T_y = bT_x^a$. The one-sigma uncertainties in a and b are typically 0.010 and 0.015, respectively. The dashed curve is the line of equality, while the solid line is the linear, least-squares best fit to the data.

by looking for a systematic difference between spectral temperatures in different energy bands. All of these satellites have effective upper limits comparable to the spectrum shown in Figure 3 thanks to the relative scarcity of ICM photons above 10 keV. The *Einstein* MPC temperatures of David *et al.* (1993) are available for many clusters and use a consistent lower limit of 2 keV, so we use this data set as our basis. Each of the other three satellites makes some use of photons below this threshold, and should therefore return cooler temperatures than the MPC. The *EXOSAT* temperatures (Edge & Stewart 1991) used here are derived from Raymond-Smith spectral fits in the range 1.5-9.0 keV, with an additional constraint coming from unresolved soft photon counts in the approximate range 0.6-1.0 keV. *Ginga* spectra (Hayakude 1989) have an energy range of 1-20 keV for cluster observations (Arnaud *et al.* 1991) and typically obtain a single significant bin below 2 keV.

Some comparisons between the results of these satellites have already been made in the literature. David *et al.* (1993) found reasonable agreement between MPC, *EXOSAT*, and *Ginga* temperatures, and note that *EXOSAT* temperatures are typically 0.7 keV less than their MPC temperatures for clusters between 5 and 8 keV. They also find reasonable agreement between *Ginga* and MPC temperatures, but fail to note that out of 8 clusters only one of the *Ginga* temperatures is higher than the MPC determination. More telling evidence comes from an analysis of *ASCA* data. Markevitch *et al.* (1998) state that *ASCA* temperatures determined in the [0.5,11] keV bandpass were typically lower by about 0.5 keV than temperatures determined in other ranges. Markevitch *et al.* use the [1.5,2]+[2.5,11] bandpass for their published temperatures in an effort to avoid this systematic (the hole in the spectrum avoids a region with a difficult point spread function), and found good agreement between their temperatures and those of other satellites.

If an excess of soft photons is really making the ICM appear cooler than it is, we should expect that the MPC has the hottest spectra because it has the highest minimum energy. We thus collect temperatures from the literature (*EXOSAT*: Edge & Stewart 1991; *Ginga*: Hatsukade 1989 via David *et al.* 1993; MPC: David *et al.* 1993; *ASCA*: Markevitch *et al.* 1998) and make our own comparison to see if this is true. There is good overall agreement between *ASCA* and *MPC* temperatures, but the gap in the *ASCA* spectrum makes comparison of the techniques difficult; we therefore do not include these data in our analysis. The *EXOSAT* and *Ginga* temperatures used here, however, each make use of the full [2,10] keV band as well as including constraints from photons below 2 keV. These temperatures are plotted in Figure 6, and are for the most part *lower* than the MPC measurements. While in most cases the error bars intersect the line of equality, the probability that so many of these observations scatter below the line is quite small and argues for some systematic error. Assuming that the clusters are drawn from an unbiased distribution in which each object has equal probability to fall above or below the line of equality, this uneven arrangement of clusters (4 above, 12 below) has only a 4% chance of occuring at random. It is also interesting to note that all the clusters whose vertical error bars fall short of the line are in the "cool" direction predicted by these simulations.

The observational evidence, though far from conclusive, suggests that the influence of line emission in the [0.5,2] keV range is not negligible. If true, a conservative response would be to adopt the [2-10] keV band as a standard for spectral temperature determinations. Judging from Figures 1 and 3, this would remove most of the excess soft photons from the spectrum and reduce the bias due to cool gas. We test the effectiveness of this technique by fitting our cluster spectra in the [2.0,9.5] bandpass while maintaining a 20,000 photon normalization over the entire energy range. The results of this analysis are shown in Figure 7; throwing out all the photons below 2 keV results in temperatures driven primarily by the Bremsstrahlung component, and the spectral temperatures are now much closer to the mass-weighted measure.

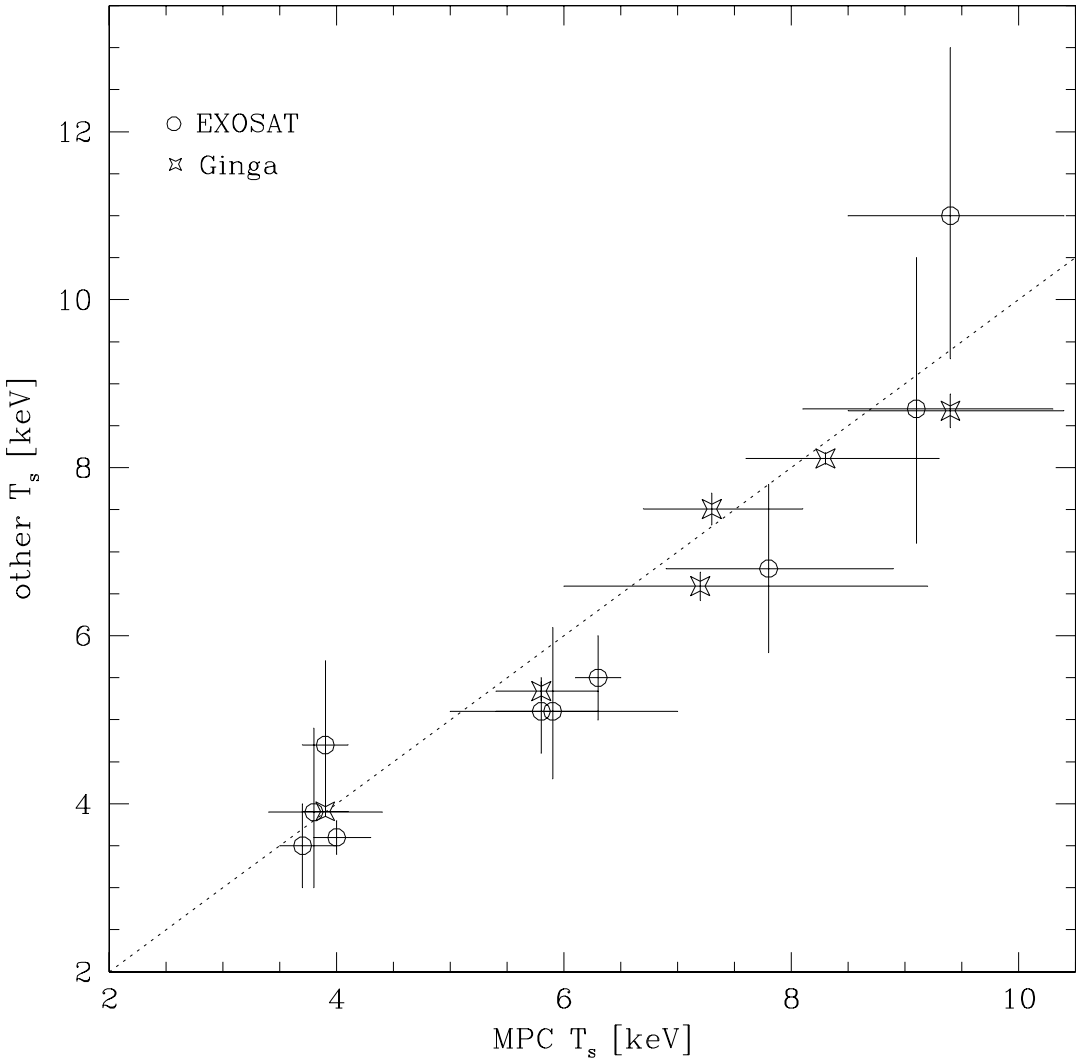

Fig. 6.— Comparison of previously published cluster temperatures from the *Einstein* MPC, *EXOSAT*, and *ASCA*. The MPC temperatures are best-fit spectral temperatures in the [2,10] keV band, and the other two satellites each make some use of photons below 2 keV. All error bars represent 90% confidence intervals. Clusters with poorly determined MPC ($\delta T > 2.0$ keV) temperatures are left out because their error ranges easily overlap the line of equality and their inclusion makes the plot difficult to read. The probability that only 4 of the 16 data points scatter above the line is only 4%, assuming the temperature determinations are equivalent.

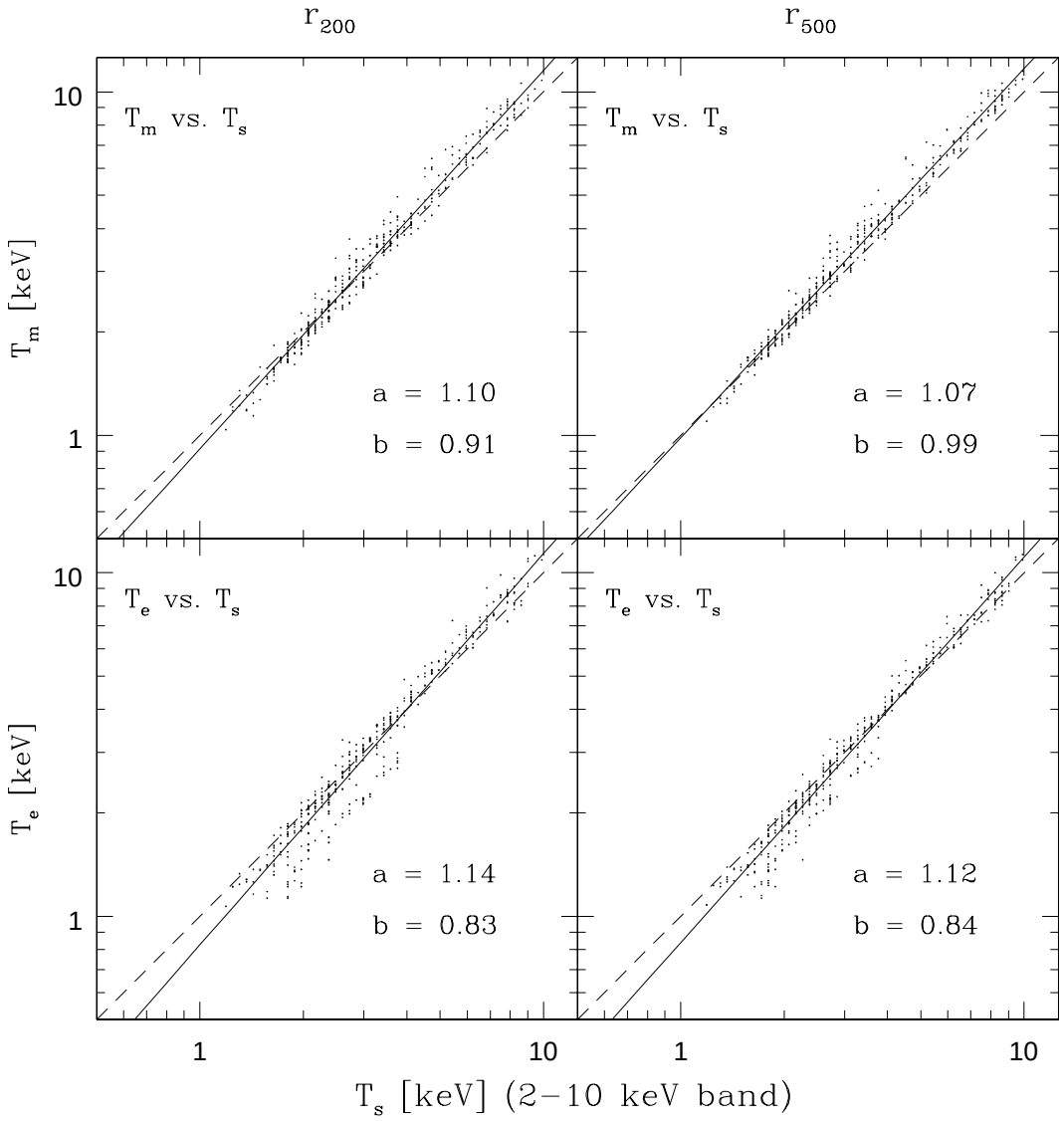

Fig. 7.— Correlations between spectral, mass-weighted, and emission-weighted temperatures for the cluster outputs. These plots can be read in the same way as those in Figure 5, except here spectral temperatures are calculated by fitting the spectrum in the [2.0,9.5] keV bandpass.

Another view of this analysis is given in Figure 8, which shows the fractional differenct $(T_m - T_s)/T_s$ plotted against the spectral temperature for four methods. This plot makes it easier to estimate the size of the errors and their scale-dependence. We see that the [0.5,9.5] keV spectral temperatures almost universally underestimate the mass-weighted temperatures, typically by 10-20% but sometimes by as much as a factor of two. We see similar results within r_{500} and r_{200} for these spectra. The picture looks brighter in the [2.0,9.5] keV bandpass, with almost all the errors confined within ±20%, but the scale-dependence of the effect is stronger. The panel which corresponds most closely to real measurements is the [2.0,9.5] bandpass temperature for emission within r_{500}, in the lower right of the Figure. The best-fit line drawn through these points follows the equation

$$\delta T_s \equiv \frac{T_m - T_s}{T_s} = (0.19 \pm 0.02) \log_{10} T_s[\mathrm{keV}] - (0.016 \pm 0.010). \quad (7)$$

The uncertainties are at the one-sigma confidence level. We thus find that even in this bandpass the temperatures of hotter clusters are underestimated by 10-20%. Although gross deviations are rarer, there are still a few cases where the mass-weighted temperature is 40% higher than the spectral temperature. From here on, when we use the term "spectral temperature" we refer to the temperature measured within r_{500} in the [2.0,9.5] keV bandpass, unless otherwise noted.

Before going on, we point out a few effects which are potentially important but beyond the scope of this work. First, it seems a likely possibility that electron temperatures are much lower than ion temperatures in the cluster outskirts. Chièze *et al.* (1998), who performed an Eulerian simulation of the ICM for a Coma-like cluster, found little difference in the two temperatures within r_{500} but about a 20% difference between the two at r_{200}. Takizawa (1999) performed head-on collisions of merging clusters designed to produce a final state of 8 keV and found similar results. Because the Coulomb relaxation time scales as $T^{3/2}$, any nonequlibrium thermodynamic signal would affect the scale-dependence of the temperature errors described in Figure 8. However, the magnitude of this effect is likely to be small, especially within the higher density r_{500} window.

A second effect which may be important in some clusters is the absorption of soft X–rays by galactic hydrogen; if this absorption factor is strong enough the influence of bins below 2 keV on the fit can be greatly reduced. Applying a photon absorption model appropriate for a column density of $3.4 \times 10^{20}\mathrm{cm}^{-2}$ to our spectra and rederiving Figures 5, 7, and 8, we find no significant change in the best-fit parameters for these correlations. However, a column density of $10^{21}\mathrm{cm}^{-2}$ is sufficient to change the behavior of the spectral temperatures. The best-fit parameters for Figure 5 under this level of absorption become $T_m = 1.06T_s^{1.03}$ and $T_e = 0.96T_s^{1.06}$ within r_{200}; and $T_m = 1.12T_s^{1.00}$ and $T_e = 0.95T_s^{1.06}$ within r_{500}. The results for the [2.0,9.5] keV band spectral temperatures are unchanged under both absorption models.

We close this section with a brief discussion of preheating. The slope of the L_X–T relation in cooling-flow corrected clusters is well-constrained observationally to be 2.64 +/- 0.27 (Markevitch 1998), a value significantly different from the slope of 2 predicted by models of self-similar gravitational collapse. Simulations which preheat the baryons at an early epoch impose a minimum entropy on the ICM during cluster formation and have been able to better reproduce the observed slope (Cavaliere *et al.* 1998; Bialek, Evrard & Sulkanen in preparation). If preheating proves to be important, the density (and therefore emissivity) of very cool infalling gas will be limited and its influence on the spectrum reduced. Two such thresholds are plotted in Figure 4 to illustrate this effect. These lines represent minimum entropies (defined as $T/n_e^{2/3}$) of 60 and 120 keV cm^2, reported in a paper by Lloyd-Davies, Ponman, & Cannon (2000) which directly measures the entropy in 20 cluster cores, including 4 groups with spectral temperatures below 1 keV. Because the baryon fraction in these simulations is about a factor of two higher than observed ICM

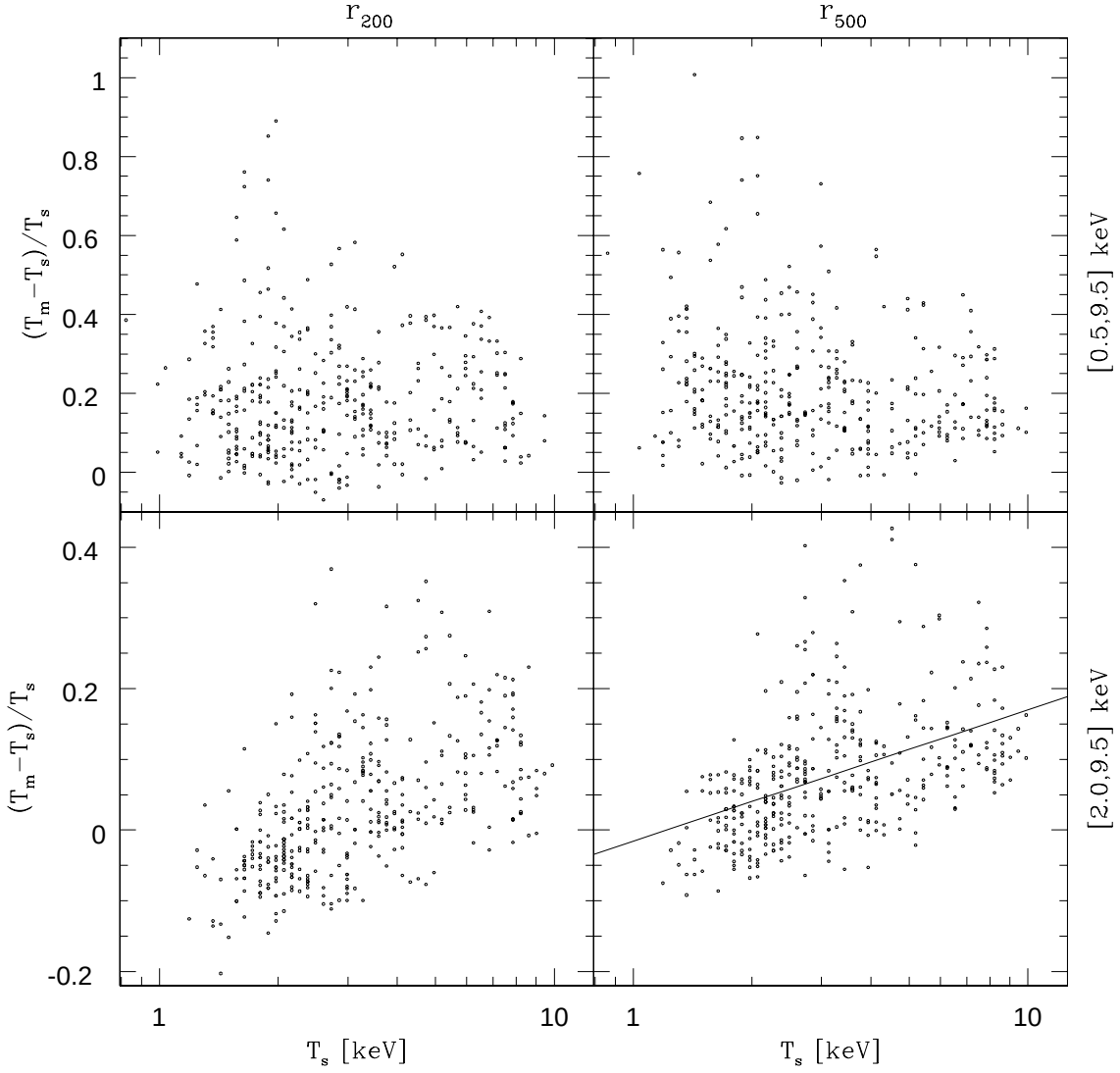

Fig. 8.— The fractional difference between spectral and mass-weighted temperatures as a function of T_s for four different methods. The upper plots measure T_s within the [0.5,9.5] bandpass, while the lower plots measure T_s within the [2.0,9.5] bandpass.

mass fractions, we rescale these entropy thresholds by a factor of $2^{-2/3}$ to 40 and 80 keV cm^2.

The effect of preheating on our results is difficult to assess without recourse to another simulation ensemble, but we can estimate the magnitude of this effect by assigning each particle violating the upper threshold the maximum allowed density at its temperature. Applying this technique to the cluster displayed in Figure 4 results in a spectrum with best-fit temperatures $kT_s = 7.5$keV (an increase of 15%) in the [0.5,9.5] keV band and $kT_s = 8.2$keV (an increase of 4%) in the [2.0,9.5] keV band. We can conclude that a large degree of preheating has the potential to reduce the deviation between spectral and mass-weighted temperatures, especially in the [0.5,9.5] keV band. We defer further analysis of this question in anticipation of a preheated simulation ensemble calibrated to reproduce the observed scaling relations (Evrard, Mohr *et al.* , in preparation).

3.2. Observable Consequences

The results of the previous section make clear two important points. First, spectral temperature determinations tend to be lower than the underlying mass-weighted temperature. Because of this bias, an analysis of the population which makes use of spectral temperatures and the virial relationship will underestimate the binding masses of rich clusters by 15-30%. Second, the exact nature of the systematic is dependent on the bandpass used in spectral fitting. A simple test of this dependence can be easily made with Chandra data by comparing [0.5,9.5] keV band temperatures to [2.0,9.5] keV band temperatures. Predictions for this effect from the simulation ensemble are shown in Figure 9. The solid line in this figure is the linear least-squares best fit to the points, and follows the relation

$$kT_{s,[0.5-9.5\mathrm{keV}]} = (0.81 \pm 0.01)\ kT^{1.09\pm0.01}_{s,[2.0-9.5\mathrm{keV}]}. \quad (8)$$

An interesting side effect of this spectral modeling becomes apparent when we create azimuthally averaged surface brightness profiles for our simulations in the [0.5,2.0] keV bandpass. Analysis of *ROSAT* position sensitive proportional counter (PSPC) images has shown that cluster emission profiles are generally well fit by a beta-model with an average slope parameter β of 0.64 (Mohr *et al.* 1999, this paper is referred to as MME in this section); this value is consistent with previous analyses and the canonical value $\beta = 2/3$. The value of this parameter has been a challenge for simulations, which have traditionally produced much steeper emission profiles. An earlier generation of surface brightness images created from this ensemble, for example, produced profiles which were well fit by a beta-model but with $\langle\beta\rangle = 0.83$; such results are typical in the field (e.g. Eke *et al.* 1998), but not often discussed.

Simulated clusters have moderate temperature profiles; the (mass-weighted) ICM temperature at r_{500} is typically between 80 and 90% of the mean temperature within this radius. The gas in the outer regions also tends to exhibit wider variations in density and temperature (Mathiesen *et al.* 1999), and pockets of gas much cooler than this can be found in most clusters. The luminosity of simulated clusters is generally modeled with a bremsstrahlung spectrum, which is rather insensitive to temperature in a soft X–ray band such as the [0.5,2.0] keV used to analyze PSPC images in Mohr *et al.* When a spectral model including line emission is used instead, we find that cool gas in the outskirts of the cluster (including the very cool gas near the virial radius which lies along our line-of-sight) significantly enhances the luminosity in this band. The mean β-parameter for our ensemble's spectral profiles is 0.59, and corresponds much more closely (in both value and process) to observed clusters. This sudden reversal of a long-standing discrepancy between simulations and reality emphasizes the importance of interpreting simulated data with a realistic "observational" framework.

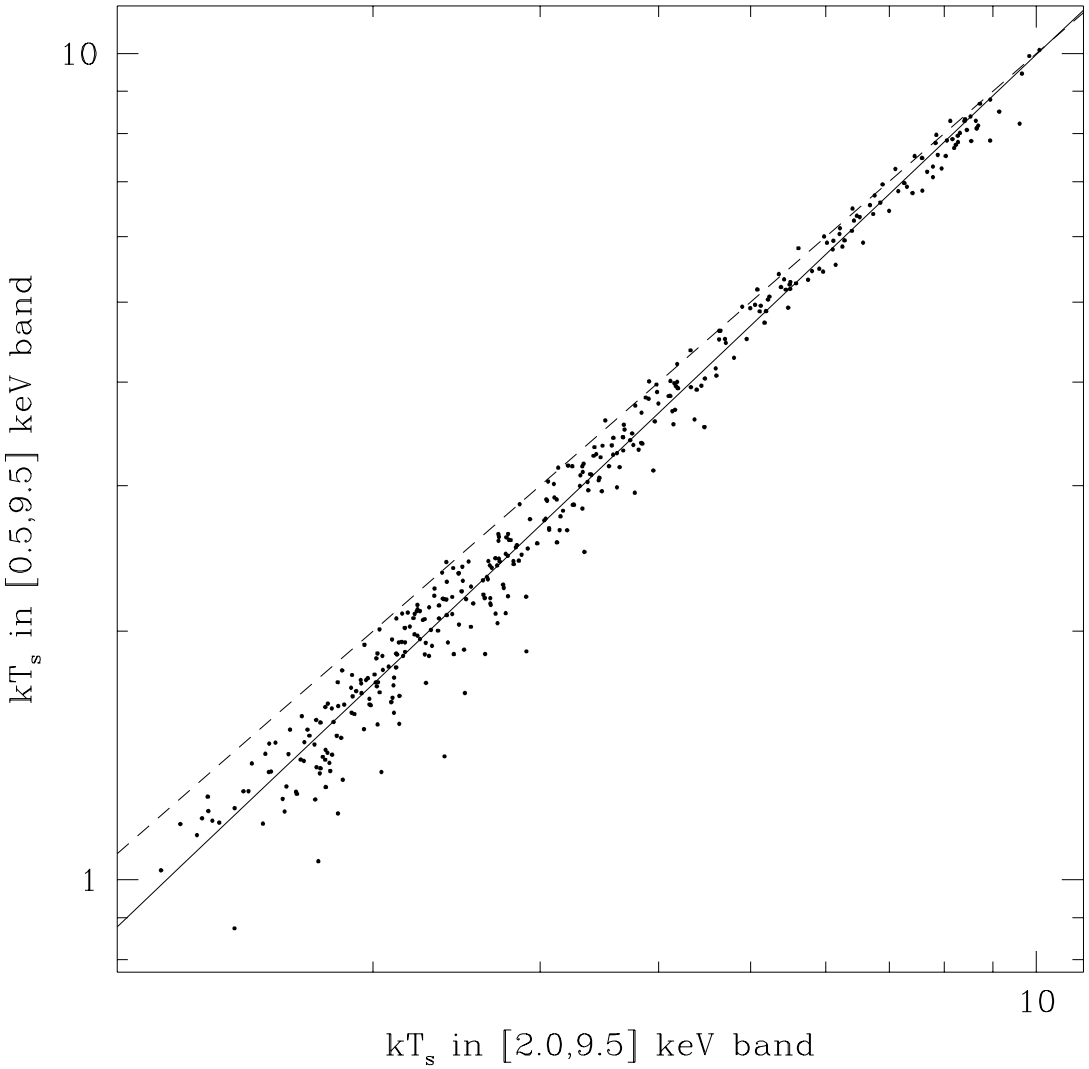

Fig. 9.— The relationship between spectral temperatures fitted in the [0.5,9.5] keV and [2.0,9.5] keV bandpasses. This relationship should be reproducible with Chandra ICM observations. The solid curve is the best-fit line described in the text, and the dashed is the line of equality. The mean scatter around the best-fit relation is 0.033 in $\log(kT)$, or 8%. The temperatures are calculated within r_{500}. The best-fit relation within r_{200} has a slightly smaller slope (1.06 rather than 1.09) but the same normalization and scatter.

The scale dependence of deviations in the spectral temperature will tilt the virial mass-temperature relationship. The relationship between spectral temperature and total cluster mass derived from three output epochs of the simulations is displayed in Figure 10. This correlation has a significantly higher slope and somewhat larger scatter than that displayed in Figure 2. The best-fit $M_{\rm tot}$–T relation for these data has a slope of 1.62 ± 0.07 (90% confidence level). The baryon fractions of our simulated clusters within r_{500} fall in the range 0.181 ± 0.007 (the global fraction is 0.2) and are independent of mass, so for us $M_{\rm tot}$ and $M_{\rm ICM}$ are essentially equivalent. This result can therefore be compared directly to the recent result of MME, which measured the slope and scatter of the intracluster medium M–T relationship in nearby clusters and found a slope of 1.98 ± 0.18. The degree of scatter in the two relations is similar; MME found a scatter of 17%, and the simulations display a scatter of 20%.

The result displayed in Figure 10 implies that some of the observed deviation from the virial relationship can be explained by invoking a normal incidence of both obvious and hidden substructure, including both major mergers and the minor accretion events which are typical of any epoch. Since both Figure 10 and the result of MME depend on the spectral temperature, their slopes can be compared directly. Combining these two results, we can infer a mild temperature dependence in the ICM mass fraction of the form $f_{\rm ICM} \propto T^{0.36\pm0.19}$. This is wholly consistent with the directly observed variation $f_{\rm ICM} \propto T^{0.34\pm0.22}$ reported by MME. To put it another way, the variation in $f_{\rm ICM}$ with temperature observed by MME is not strong enough to account for the observed difference between the $M_{\rm ICM}$–T relation and the virial relation. It is, however, strong enough to match the $M_{\rm tot}$–T_s relation found in this paper.

We report the best-fit $M_{\rm tot}$–T relationships from these simulations for all our definitions of temperature in Table 3.2. While the mass-weighted and [0.5,9.5] keV band spectral temperatures are consistent with the virial relation, the [2.0,9.5] keV band and emission-weighted temperatures are not. It is important to emphasize that the emission-weighted temperature used in this paper is not an observable quantity, and there is no evidence to suggest that it is comparable to the observer's definition. Further work with these simulations needs to be done to reproduce an observable version, for example the flux-weighted average of spectral temperatures observed in each image pixel.

This analysis seems to imply that the best way to measure temperatures with *Chandra* is to limit spectral fits to photons of 2 keV or greater energy; the temperature that results will not only be closer to the mass-weighted temperature, but will also be comparable to previous determinations. There is a price to pay, however, for rejecting the abundant low-energy photons. As we will see in the next section,

Temperature	r_{500}			r_{200}		
definition	$\log M_{15}$	a	σ_M	$\log M_{15}$	a	σ_M
T_m (mass)	-1.34 ± 0.02	1.52 ± 0.03	0.058	-1.17 ± 0.03	1.54 ± 0.05	0.097
T_e (emission)	-1.20 ± 0.03	1.38 ± 0.05	0.10	-1.05 ± 0.04	1.39 ± 0.07	0.15
T_s (0.5-9.5 keV)	-1.21 ± 0.04	1.48 ± 0.07	0.14	-1.04 ± 0.04	1.51 ± 0.08	0.15
T_s (2.0-9.5 keV)	-1.34 ± 0.02	1.62 ± 0.04	0.081	-1.19 ± 0.03	1.64 ± 0.06	0.10

Table 1: Mass-temperature relationships, defined as $\log M_{\rm tot} = \log M_{15} + a \log kT[{\rm keV}]$, for all definitions of temperature used in this paper. The parameters M_{15} (mass in units of $10^{15} M_\odot$) and a are calcuated from the linear least-squares equation based on the scatter σ_M in $\log M$ around the relation. The uncertainties represent a one-sigma confidence interval.

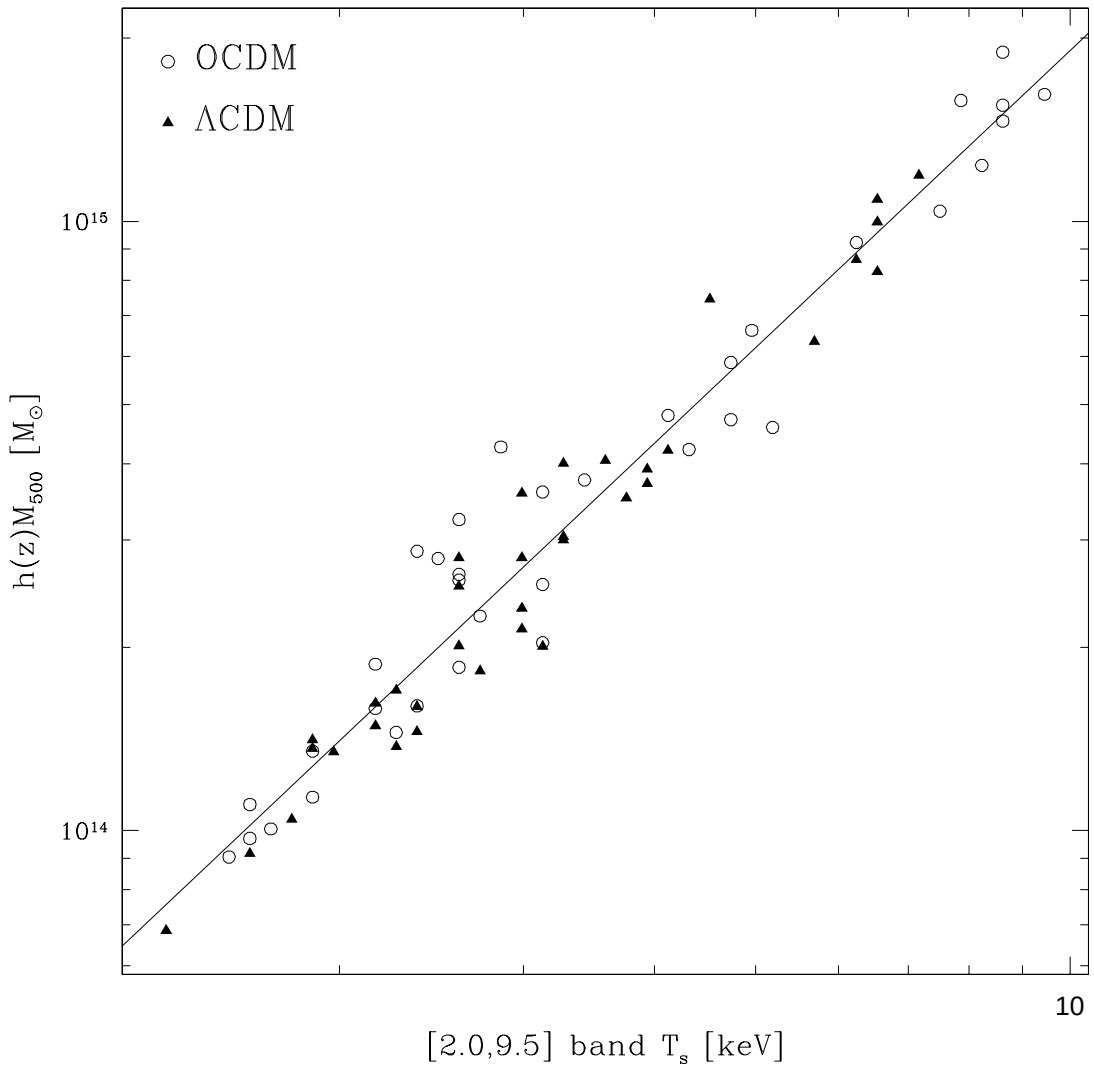

Fig. 10.— Cluster mass vs. spectral temperature for simulated clusters. The solid line is the least-squares fit to the data, and the corresponding equation is given in Table 3.2. The scatter in $\log M$ at fixed T_s is 0.081, or 20%. Three output frames for each cluster are included in the plot, corresponding to z = 0, 0.5, and 1. A similar result with slightly larger scatter is obtained for measurements within r_{200}.

the simulations lead us to expect the presence of very cool gas not just in cooling flows but also in the outskirts of the cluster. It is well known that clusters are continually accreting smaller concentrations of matter. Since they are less massive, the gas in these subsystems is naturally much cooler than that in the cluster. These clumps of remain visible in our simulated spectral temperature maps for up to two billion years after the virial radii of the two systems intersect. Including the soft photons decreases the accuracy of spectral temperatures, but also increases the contrast between these hot and cold regions. Thus, spectral temperatures in the full *Chandra* bandpass will be more useful in determining a cluster's dynamic state.

4. Dynamics

It is logical to ask several questions at this point. First, there are several instances where the spectral temperature underestimates the mass-weighted temperature by a considerable degree. If these excursions are the result of cluster dynamics, we should be able to see evidence of unusual structure in the cluster at these points. Second, we have claimed that the reason spectral temperatures typically underestimate the mass-weighted temperature is that most clusters contain significant amounts of cold gas in their outskirts. If accretion events and mergers are driving the difference between the two temperatures, we should be able to discover a time dependence in the effect, and perhaps even relate the scale of the errors to typical accretion rates. Both of these questions are really asking the question named in the title of this paper: how are temperature measurements affected by a cluster's dynamical state?

Fortunately, the history of the simulations gives us a means to answer this question. As stated in §2, we have created spectral temperature maps for each cluster at 16 points during its evolutionary history. We have also kept track of the trajectories of dark matter groups during this evolution and used this information to determine the times at which major merger events occur. Using this information, we can create objective definitions of the cluster's dynamic age and attempt to correlate these quantities with the biases described in the previous section.

4.1. Identifying Mergers

The mergers themselves are easy to find. At each timestep we identify dark matter groups with a mass of at least 100 particles (the real mass corresponding to this threshold varies but is always a fixed fraction of the total mass in the simulation volume). By keeping track of the particle indices associated with each group, we can identify at later times which groups were absorbed into a given cluster. We identify merging groups with a mass ratio of at least 10% as "major mergers" and build up a catalogue of these events. This results in a catalogue of 75 merger events for the 24 clusters. The limiting mass ratio was chosen to strike a balance between frequency and significance; a merging subclump of 10% the primary mass can be easily seen in our temperature maps (when the viewing angle is right) as a region of cool emission behind a bow shock, but is not so common that simultaneous events are typical. A fine example, which also happens to be one of the two exceptions to this rule, is shown in Table 2, which shows the spectral temperature map of a three-way merger in the two bandpasses discussed earlier. Although the merging mass ratio is small, it is clear in this illustration that soft photons from the merging subclumps dominate the spectrum over a fairly large volume. A minor shock front is visible between the two accreting systems, but these few pixels have very little effect on the overall temperature of the cluster.

The time at which a merger occurs is a more nebulous concept than the merger's existence. The

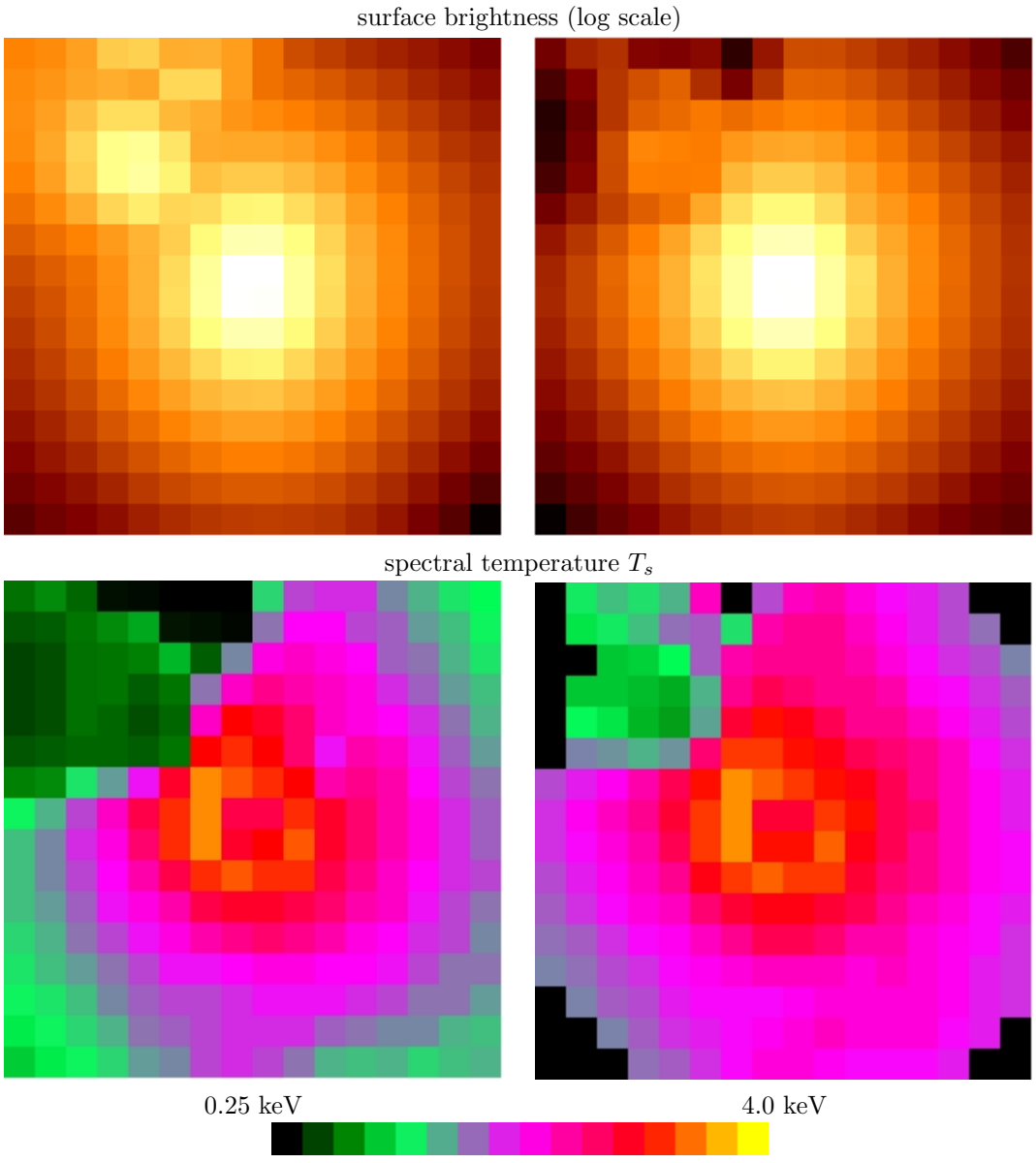

Table 2: We see here one of the smaller clusters in our sample as it goes through a three-way merger. The larger clump is 10% the mass of the parent cluster, and the smaller about 8%. In the [0.5,9.5] bandpass (left-hand side) the individual clumps are clearly distinguishable in the surface brightness image. In the [2.0,9.5] bandpass (right-hand side), however, this is not the case. In both bands, a shock can be seen forming between the subclumps in the spectral temperature map. The black pixels in the [2.0,9.5] keV T_s map contain too few photons to constrain the temperature. These images have a width of $2r_{500}$, equivalent to 1.3 Mpc for this cluster.

individual outputs are separated by about 0.6 Gy, so merely identifying this time with the first output in which two groups are merged introduces a large random error. We can, however, calculate the center of mass of each dark matter group in previous outputs and create an interpolating function for the groups' separation. This function can be used to create more accurate and objective definitions of the merger time.

Our intuitive expectation for the effect of a merger event on the ICM temperature is as follows: as the two groups approach one another, their ICMs begin to interact at a fairly large separation and we will see a shock begin to form. The gas in a typical shock is much hotter than the rest of the ICM, and should bias measurements towards higher temperatures. As the event proceeds, the main body of the merging system penetrates the virial radius of the cluster and introduces a large mass of cold gas into the image. The subclump will be more massive and more luminous than the gas in the shock, so its weight will be greater under any reasonable definition of the temperature. We thus expect to see a rapid cooling in the combined spectrum shortly after the shock forms, even though the shock may still be clearly visible in temperature maps. After some time the ICM will equilibrate and approach the virial temperature again. Most merger events involve very small mass fractions, so this process should not greatly affect mass-weighted temperatures. We can hope to observe the process of heating and cooling through a merger much more clearly in the spectral and emission-weighted measures.

Practically, we interpret this expectation by identifying a merger time t_m for each event, defined as the time at which the virial radii (r_{200}) of the two groups intersect for the first time. Identifying the merger time in this manner corresponds to the requirement that the mergers have a uniform free-fall timescale, coming together in a constant fraction of the Hubble time $t_H \equiv H_0(z)^{-1}$. Further analysis of the dark matter halo dynamics reveals that the centers of the two groups typically coincide about $0.2t_H$ after t_m.

Another relevant time scale in this problem is the time required for the ICM to approach hydrostatic equilibrium after a merger. The equilibration time is often approximated by the time required for a sound wave to traverse the cluster,

$$t_s = 2 \times 10^9 (kT)^{-1/2} D \text{ Gy Mpc}^{-1} \tag{9}$$

where kT is measured in keV and D is the diameter of the cluster (Sarazin 1986). The clusters in our ensemble have sound crossing times between 1 and 4 Gy, with a mean of 2.3 Gy. The mean time between merger events, on the other hand, is about 2.7 Gy. It would seem from this that our clusters are out of hydrostatic equilibrium for most of their total lifespan.

4.2. The Effect of Mergers

Armed with a list of 75 merger times t_m, the Hubble time t_H at each output frame, and the sound crossing time t_s in each output frame, we can proceed to look for correlations of temperature with the cluster dynamical states. We start by defining a parameter which measures the cluster's proximity to a major merger:

$$\Delta\tau_H \equiv (t - t_m)/t_H \tag{10}$$

where for each output frame t_m is taken to be the time of the *closest* merger event. $\Delta\tau_H$ can thus be either positive or negative, a freedom which reflects our uncertainly as to when the merger process will begin to influence the spectrum.

The relationship between spectral temperature errors and $\Delta\tau_H$ is striking, and is displayed in Figure 11. This Figure is constructed for clusters observed in the r_{500} window; the corresponding Figure for r_{200}

looks similar. The four different point sizes correspond to categories in the merger mass ratio: from smallest to largest they represent the ranges $m/M < 0.2, 0.2 \leq m/M < 0.4, 0.4 \leq m/M < 0.6$, and $m/M \geq 0.6$. A glance at this plot demonstrates that the mass ratio of the merger doesn't have much impact on the spectral temperature measurements. This can be understood as evidence for a balance in the roles of the subclump's temperature and luminosity in causing the bias; in a major merger event the subclump has more influence on the spectrum but its temperature is also closer to the parent system's. The fact that all of the large deviations are clustered near the $\Delta\tau_H = 0$ axis indicates that these excursions are indeed related to the merger process, and suggests a method for culling dynamically young clusters from our sample which we will return to later. The horizontal line is a visual aid to the scale of error which may be isolated from the sample, drawn so that all the points above it are isolated within a small range in $\Delta\tau_H$.

There is a single cluster in our sample which goes through one and only one major merger in its lifetime; its points are connected with a solid line in Figure 11 to serve as a benchmark for our physical intuition. Unfortunately, this cluster is not entirely typical; it is rather small and somewhat cool for its mass ($5 \times 10^{14} M_\odot$, $kT_m = 4$ keV, $kT_s = 2.8$ keV). Still, the process of apparent cooling as it goes through a merger with mass ratio $m/M = 0.38$ is rather obvious.

We can reiterate this point by defining a second dynamical time $\Delta\tau_s$ with respect to the sound crossing time of the cluster:

$$\Delta\tau_s \equiv (t - t_m)/t_s. \tag{11}$$

Although this equation looks very similar to our definition of $\Delta\tau_H$, there is an important difference: we do not allow this timescale to take on negative values. Thus the merger time used is now *always* the last merger to occur before the output time t. For outputs where no merger has yet occurred, we take the numerator to be the age of the cluster. We define the time $\Delta\tau_s$ in this manner because we are interested in time required for our clusters to come to equilibrium after a merger.

We plot the bias in spectral temperature against $\Delta\tau_s$ in Figure 12. The result is similar in that the large errors mostly occur close to a merger event and typically less than one sound crossing time distant. This suggests that the measure given in equation 9 is not just a sound dimensional estimate but actually a very good measure of the equilibration timescale. Again, the results for other bandpasses and density contrasts look quite similar.

It is interesting to note from Figures 8 and 11 that the clusters which have large temperature differences are different for the two bandpasses. In the [0.5,9.5] keV range, the spectral temperatures are more likely to carry large errors in the low-temperature clusters. In the [2.0,9.5] bandpass, we see the largest errors associated with the hottest clusters. Despite this difference, however, we see in Figure 11 and its equivalents that the largest errors in both bandpasses are associated with merging clusters, and moreover are concentrated in an interval about $0.2t_H$ wide after $\Delta\tau_H = 0$.

This tells us that merging clusters, and only merging clusters, are likely to carry large temperature errors, but the different bandpasses select clusters in different mass ranges. In the [2.0,9.5] band the fit is driven almost entirely by the effective slope of the bremsstrahlung component. This slope varies rapidly at low temperatures, and the spectrum of a blob of colder gas will be swamped by that of the parent. At higher temperatures (for example, a 9 keV parent and a 5 keV satellite) the mixing of exponential tails is more likely to produce a significantly cooler spectrum. In the [0.5,9.5] keV band, however, there is more balance between the soft and hard photons. Between 0.5 and 2.0 keV the spectrum will be driven by the merging subclump, while in the brehmsstrahlung tail the spectrum will be driven by the parent cluster. The tug-of-war between the two regimes is decided by the number of bins in the spectrum, so in this bandpass

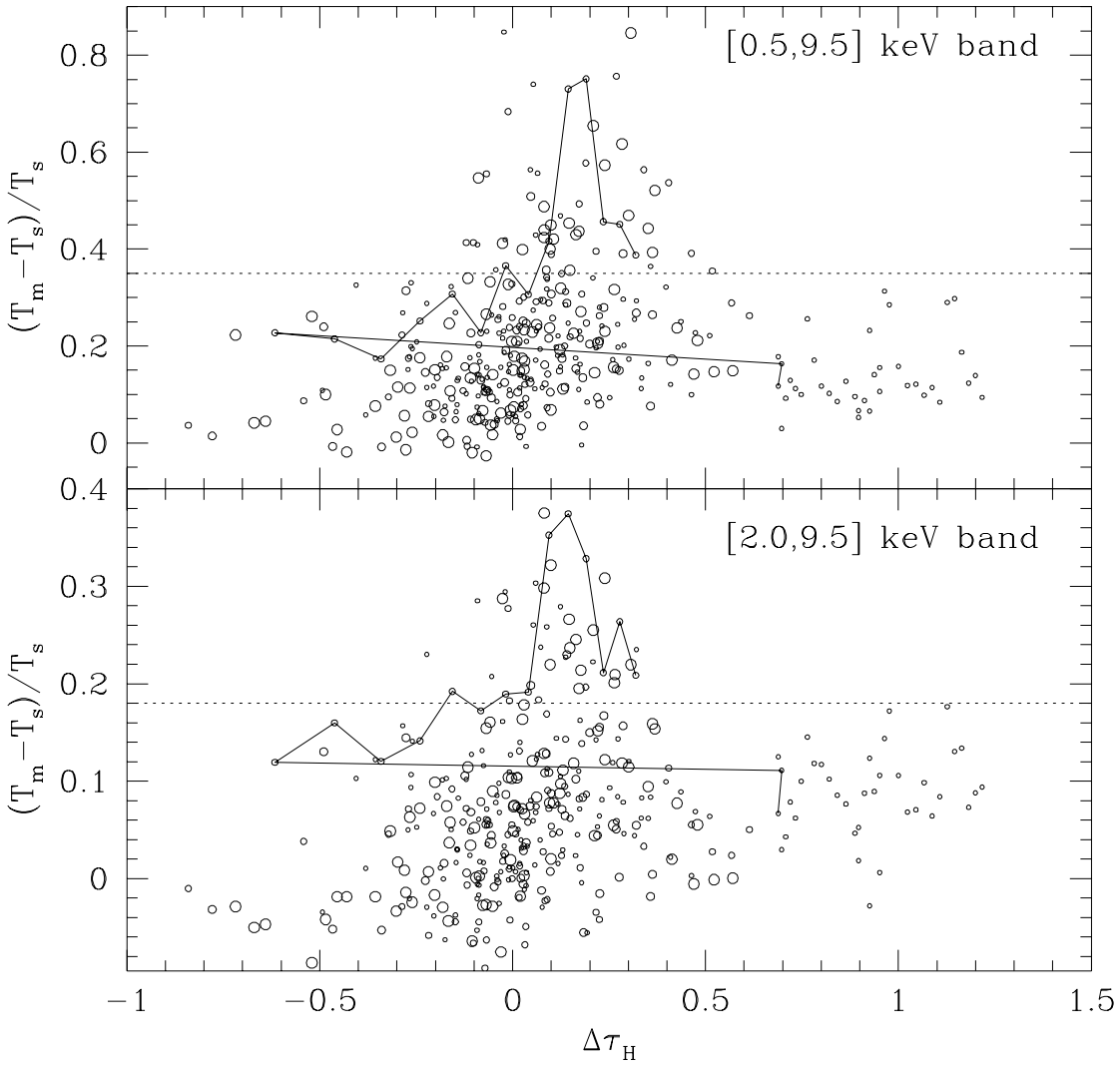

Fig. 11.— The fractional deviation in spectral temperature as a function of $\Delta\tau_H$. This figure and the variables displayed are described in detail in the text. The point sizes increase with the mass ratio of the closest merger event, and the connected points correspond to the only cluster in our sample which goes through just one merger in its lifetime. The horizontal dotted lines are visual aids to help separate the regions of large errors close to a merger event.

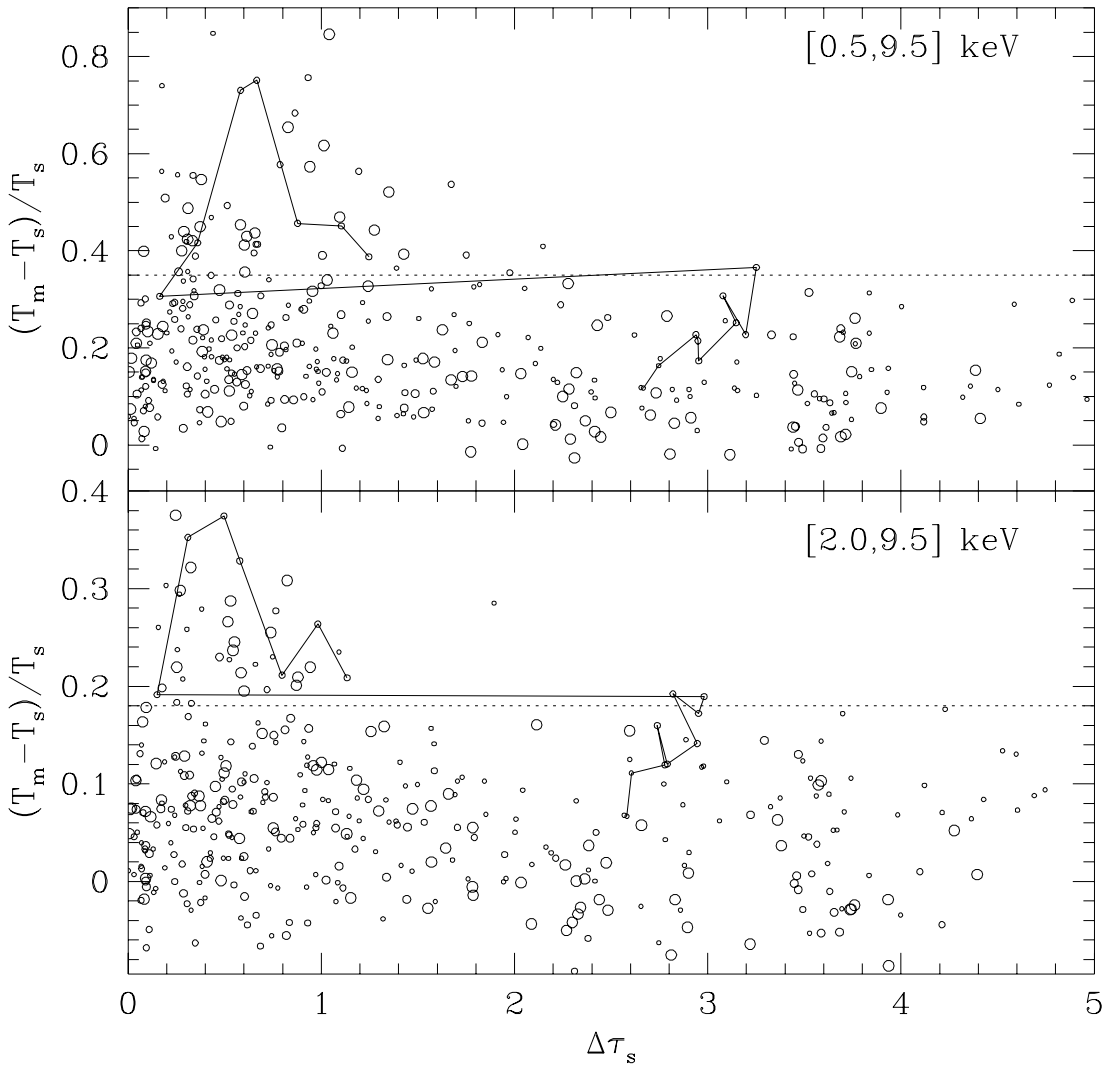

Fig. 12.— The fractional deviation in spectral temperature is plotted against $\Delta\tau_s$, as described in the text. Most of the large differences occur in frames less than one sound crossing time after a merger event, especially in the [2.0,9.5] keV bandpass. These temperatures are also measured within r_{500}.

the hottest clusters are better able to resist the influence of a cool component.

4.3. Culling Mergers

We have seen in the previous sections that a simulated cluster ensemble, with realistic incidence of substructure, displays spectral temperatures with a significant and scale-dependent systematic bias. The largest deviations between spectral and mass-weighted temperatures come from clusters which are dynamically young: they are either about to undergo or have just undergone a major merger and the presence of cool gas in the observation window changes the shape of the combined spectrum. Some of these mergers will be easily identifiable with *Chandra* through the temperature structure of the gas, displaying images similar to those displayed in Table 2. Others will be invisible, however, hidden behind the main body of the cluster but still significantly altering the spectra. We would like to develop a method for identifying some or all of these, so that mass-weighted temperatures and cluster binding masses can be determined through X–ray observations with a minimum of error. Our expectation is that a large sample of cluster observations, culled of all of obvious mergers and some inobvious mergers, will reflect the virial relations better and allow us to more accurately measure variations in baryon fraction, deviations from self-similarity, and constraints on the power spectrum.

The results of the previous section tell us that the clusters with spectral temperatures much colder than the mass-weighted temperature always lie close to a merger, although the reverse is certainly not true. We are left with little else to go on: the deviation in spectral temperature is uncorrelated with either merger mass fraction (a bit suprising) and shows no dependence on the cosmological model. It does show some dependence on the mass of the parent, which leads to a change in slope of the observed mass-temperature relation. Figures 11 and 12 of the previous section are not observables, since we can't yet reliably identify merger events. We would like to cull the largest excursions from a real cluster sample, but we need to do it some other way.

The solution is to build up an observable mass-temperature correlation (or ICM mass, if you prefer; remember that the fixed baryon fraction in our simulations makes the two equivalent) and cull out the clusters which are coolest *relative to the mean relationship*. We have already plotted the cluster mass vs. spectral temperature for the [2.0,9.5] bandpass within r_{500} in Figure 10. Our analysis leads us to expect that the clusters which fall far below the best-fit line may be merging clusters. To test this we treat mass as the independent variable, and calculate the difference between T_s as measured and the predicted T_s based on the best-fit correlation with cluster mass. This quantity is then plotted against $\Delta\tau_H$, as defined in the previous section.

The results for the [0.5,9.5] bandpass within r_{500} are displayed in Figure 13. We've switched bands here because the culling technique we propose seems to work best when temperatures are measured over the entire energy range (due to the increased contrast mentioned above). This plot is harder to interpret, but by drawing a horizontal line we see that we can isolate the 40 (10%) coolest (relative to the expected temperature at that mass) images and be reasonably sure that these clusters are dynamically young, i.e. $-0.1 \lesssim \Delta\tau_H \lesssim 0.4$. In real life, we could apply this technique by (1) measuring ICM gas masses with precision in a soft bandpass such as that of the *ROSAT* PSPC where the luminosity is a weak function of temperature (e.g. Mohr *et al.* 1999); (2) measuring spectral temperatures with *Chandra*; and (3) culling clusters from the sample which deviate by more than -20% from the mean relation. Needless to say, this would work best with a large survey and would require a large time investment–but the remainder of the

sample would suffer less bias from clusters which are dynamically young.

Note that the definition of "dynamical youth" defined above is empirically driven. At low redshifts, 40% of the Hubble time is a generous 3-5 billion years, typically about twice as long as the freefall ($\sim 0.2t_H$) and sound crossing timescales. We adopt this definition solely because all of the clusters with large temperature errors fall within this range, without further justification, since our main interest lies in removing the least accurate measurements from our sample. Out of the whole ensemble of 384 images, fully 70% lie within this range of dynamical states.

It is also interesting to note that the hottest spectra occur either long after a merger event or at times $\Delta\tau_H \lesssim 0.2$. The free fall time from r_{200} is about $0.2t_H$, so the time interval from $\Delta\tau_H = 0$ to $\Delta\tau_H = 0.2$ represents the time required for a merging system to completely enter the observation window. The equivalent plot for $\Delta\tau_s$ is not given here, but again shows that most of the clusters below this cut are dynamically young. ($\Delta\tau_s \lesssim 1$). A similar result is found in constructing these plots with the emission-weighted temperature, except there is also mild evidence for shock heating in temperatures determined previous to $\Delta\tau_H = 0$.

Finally, we apply this analysis to the three-redshift subset of our images and their mass-temperature relationship. Figure 14 plots spectral temperature against total mass in the [0.5,9.5] band within r_{500}, draws the best-fit line and a cut on clusters 15% cooler than this line, and identifies those clusters which are dynamically young with a different symbol. We can see from this plot that the proposed cut preferentially selects out merging clusters, although there are still many left in the sample. A previous analysis of these simulations (Mathiesen *et al.* 1999) determined that ICM masses of regular clusters are measurable with only $\sim 5\%$ scatter and $\sim 10\%$ bias using the parametric technique of Mohr *et al.* (1999), and more importantly that the degree of error in $M_{\rm ICM}$ is uncorrelated with mass and temperature. This culling method would therefore be unchanged if we attempted to apply it to the observable $M_{\rm ICM}$–T_s relationship.

This cut does not change the slope of the observed M–T_s relation and has a small (about 0.5 sigma) effect on the normalization. This method is thus primarily useful for identifying a subset of dynamically young clusters in a sample, presumably in the hopes that some will be found which aren't obvious in other ways. We have selected out ten merging clusters and a single relaxed object; analysis of Figure 13 implies that this ratio would be similar in a larger sample.

5. Conclusions

The first (and perhaps the most suprising) result of this paper is the revelation that the emission spectrum of a realistically complex intracluster medium is barely distinguishable from that of an isothermal gas, even over a broad spectrum. This correspondence arises because we have created spectra with rather coarse (150 eV) bins in an effort to match our observation model to *Chandra's* ACIS instrument. We provide relationships between spectral, emission, and mass-weighted temperatures in two different bandpasses and within two density constrasts; in particular, we find that spectral temperatures determined in the [2.0,9.5] keV range within r_{500} are very similar in nature to those determined by the *Einstein* MPC, *Ginga*, and *EXOSAT*. The other bandpass, [0.5,9.5] keV, is designed to be similar to *Chandra* observations, and can be used to better interpret its results.

We find that realistically determined spectral temperatures are commonly 10-20% lower than the mass-weighted temperatures in these simulations, a fact which has important implications for cluster

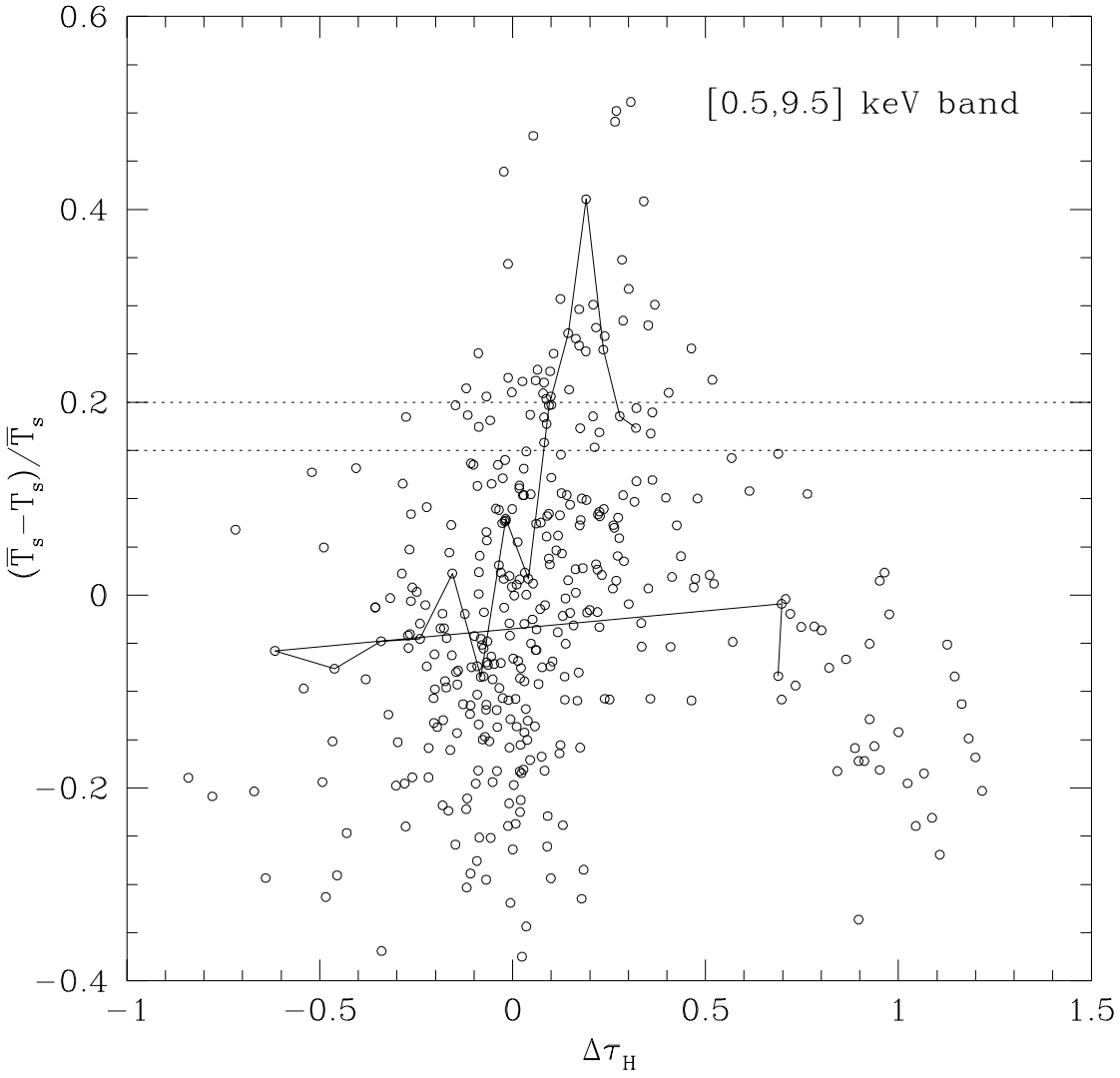

Fig. 13.— The fractional difference between T_s and $\bar{T}_s$, the spectral temperature expected from the best-fit line for that mass, is plotted against dynamical time. Again, the clusters which are coolest relative to the mean relation are clustered in the approximate range $-0.1 < \Delta\tau_H < 0.4$. This plot implies that merging clusters can be culled from a sample in a statistically well-defined way by observing the mass-temperature relation and making a similar cut on the data. The spectral temperatures used here are measured within r_{500} in the [0.5,9.5] bandpass.

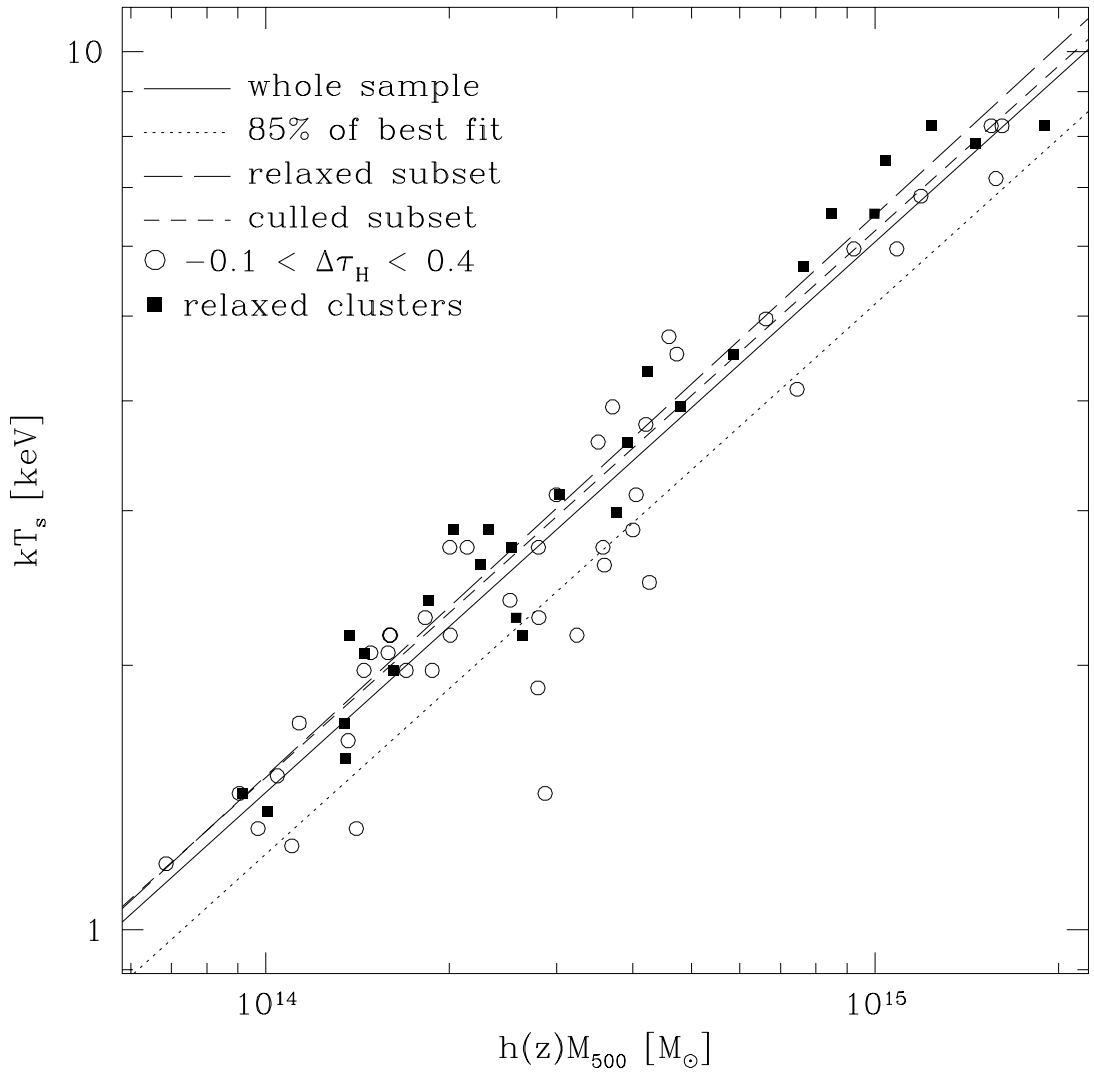

Fig. 14.— The culling method implied by Figure 13 and described in the test is demonstrated on a subset of images corresponding to redshifts 0, 0.5, and 1.0. The solid line is a fit to the entire sample (as reported in Table 3.2); the dotted line has the same slope but a temperature normalization 15easy to see from this plot that most of the clusters below the best-fit line lie close to a merger event, and performing a cut on clusters which are cool relative to the fit preferentially selects for such objects. Also plotted are linear fits to the subset of "relaxed" clusters (black squares), and the subset of clusters above the dotted culling threshold.

physics. The bias arises through the natural and frequent occurence of minor accretion events: small clumps of cool gas which merge into the ICM and produce an excess of soft X-rays, biasing the spectrum towards cooler temperatures until they are fully assimilated. Because the mass-weighted temperature follows the virial relationship, it is a more accurate indicator of the binding mass. Previous measurements of the cluster mass function power spectrum need to account for this source of error if they make use of spectral temperature data. We have calibrated the relationship between spectral and mass-weighted temperature for the [2.0,9.5] keV bandpass within r_{500} for this purpose; this should allow an appropriate correction for clusters observed by satellites with a similar energy range.

The scale-dependent nature of this bias changes the slope of the observed $M_{\rm ICM}$–T_s relationship in a direction consistent with recent determinations, but it does not account for the whole difference. Additional physics, such as a variation in the ICM mass fraction with temperature, is still needed to explain the observed slope.

Although we are stuck with a discrepance between observed temperatures and mass-weighted temperatures, this bias can be useful in identifying clusters which are dynamically young. Not all of these events will be obvious, even with *Chandra's* high-resolution surface brightness and temperature maps; some of the mergers will be occuring on an axis near our line-of-sight. In such cases the shocks and cool regions will probably be masked by core emission, but the presence of a cool subclump can still produce an unusually large deviation in the spectral temperature. We should not fall into the trap of assuming that a cluster is relaxed because it looks spherically symmetric; rather, we should do everthing we can to determine whether or not it is truly relaxed. The simulations show that all of the clusters with temperatures falling far ($\gtrsim 15\%$) below the mean mass-temperature relation are dynamically young; a subset of merging clusters can thus be identified as outliers in the observed relation.

The results described in this paper are a necessary step towards accurately measuring cluster masses under the assumption of virial equilibrium, as well as towards a reliable technique for determining a cluster's dynamical state observationally. It is not, however, the only step: first the astronomical community must recognize that the various definitions of temperature in common use are *not* equivalent. Further work needs to be done in modeling observed temperatures (e.g. core-excised spectral temperatures and flux-weighted temperatures averaged over an image) and the effects of substructure on observable quantities. Spectral modeling of simulations is computationally more expensive, but not difficult, and the level of systematic error caused by inaccurate modeling is now comparable to the observational constraints on cosmological parameters.

The spectral cubes described in this paper will be made avaiable to the public on Mathiesen's research web site [1] along with higher-resolution images for the subset of images used in fitting the mass-temperature relationships, the accretion history of each cluster, and documentation describing the file format and how to model other satellite responses. Our simulations of spatially resolved emission spectra can be used to help interpret *Chandra* and *XMM* observations of real clusters, and we are sure that enterprising researchers can mine these datasets for other interesting results.

[1] http://redshift.perseus.edu/bfm

6. Acknowledgements

We would like to thank Nancy Brickman, John Raymond, Randall Smith, and Martin Sulkanen for their help in implementing the Raymond-Smith and mekal spectral models. This research was supported by NASA grants NAG5-2790, NAG5-7108, and NAG5-8458; and NSF grant AST-9803199.

REFERENCES

Allen S. W. & Fabian A. C., 1998, MNRAS, 297, 57

Allen S. W., Fabian A. C., Johnstone R. M., Arnaud K. A., & Nulsen P. E. J., MNRAS, preprint (astro-ph/9910188)

Arnaud, M. & Evrard, A.E., 1999, MNRAS, 305, 631

Bond J. R. & Efstathiou G., 1984, ApJL, 285, L45

Bryan G. L. & Norman M. L., 1998, ApJ, 495, 80

Buote D. A. & Canizares C. R., 1996, ApJ, 457, 565

Cavaliere A. & Fusco-Femiano R., 1978, A&A, 70, 677

Cavaliere A., Menci N., & Tozzi P., 1998, ApJ, 501, 493

Chièze J.-P., Alimi J.-M. & Teyssier R., 1998, ApJ, 495, 630

David L. P., Slyz A., Jones C., Forman W., & Vrtilek S. D., 1993, ApJ, 412, 479

Edge A. C. & Stewart G. C., 1991, MNRAS, 252, 414 & 428

Eke V. R., Navarro J. F., & Frenk C.S., 1998, ApJ, 503, 569

Evrard A. E., 1990, ApJ, 363, 349

Evrard A. E., Metzler C. A., & Navarro J. F., 1996, ApJ, 469, 494

Fabian A. C., Hu E. M., Cowie L. L., & Grindlay J., 1981, ApJ, 248, 47

Fabian A. C., Arnaud K. A., Bautz M. W., & Tawara Y., 1994, ApJL, 436, L63

Fox D. C. & Loeb A., 1997, ApJ, 491, 459

Gunn K. F. & Thomas P. A., 1996, MNRAS, 281, 1133

Hatsukade I., 1989, Ph.D. Thesis, Osaka University

Holzapfel W. L., Arnaud M., Ade P. A. R., Church S. E., Fischer M. L., Mauskopf P. D., Rephaeli Y., Wilbanks T. M., & Lange A. E., 1997, ApJ, 480, 449

Kang H., Cen R., Ostriker J. P, & Ryu D., 1994, ApJ, 428, 1

Knopp G. P. & Henry J. P., 1996, ApJ, 472, 125

Lacey C. & Cole S., 1994, MNRAS, 271, 676

Lima Neto G. B., Pislar V., Durret F., Gerbal D. & Slezak E., 1997, A&A, 327, 81

Lloyd-Davies E. J., Ponman T. J. & Cannon D. B., 2000, MNRAS in press (astro-ph/0002082)

Markevitch M., 1998, ApJ, 504, 27

Markevitch M., Forman W. R., Sarazin C. L., & Vikhlinin A., 1998, ApJ, 503, 77

Markevitch M., Mushotzky R., Inoue H., Yamashita K., Furuzawa A., & Tawara Y., 1996, ApJ, 456, 437.

Mathiesen B., Evrard A. E., & Mohr J. J., 1999, ApJL, 520, 21

Mewe R., Gronenschild E. H. B. M., & van den Oord G. H. J. 1985, A&AS, 62, 197

Mohr J. J. & Evrard A. E., 1997, ApJ, 491, 38

Mohr J. J., Evrard A. E., Fabricant D. G., & Geller M. J., 1995, ApJ, 447, 8

Mohr J. J., Mathiesen B. & Evrard A. E., 1999, ApJ, 517, 627

Mushotzky R. F. & Scharf C. A., 1997, ApJL, 482, L13

Nagai D., Evrard A. E., & Sulkanen M. E., 1999, MNRAS in press (astro-ph/9903308)

Navarro J. F., Frenk C. S., & White S. D. M., 1995, MNRAS, 275, 720

Sarazin C. L., 1986, *Reviews of Modern Physics*, vol. 58, no. 1

Thomas P. A., 1998, MNRAS, 299, 349

Takizawa, M. 1999, ApJ, 520, 514

Tsai, J.C. & Buote, D.A., 1996, MNRAS, 282, 77

Waxman E. & Miralda-Escude J., 1995, ApJ, 451, 451

White D. A., Jones C., & Forman W., 1997, MNRAS, 292, 419

White S. D. M., Navarro J. F., Evrard A. E., & Frenk C. S., 1993, *Nature*, 366, 429

XSPEC User's Manual: http://legacy.gsfc.nasa.gov/docs/xanadu/xspec/index.html